On the mechanism of electron-beam-induced structural degradation in ZIF-8 and its electron dose tolerance

Pritam Banerjee[1*], Kathrin L. Kollmannsberger[2], Roland A. Fischer[2], Joerg R. Jinschek[1*]

[1.] National Centre for Nano Fabrication and Characterization (DTU Nanolab), Technical University of Denmark, Fysikvej 307, DK-2800 Kongens Lyngby, Denmark.

[2.] TUM School of Natural Sciences, Department of Chemistry, Technical University of Munich, Lichtenbergstr. 4, D- 85748 Garching, Germany.

* Corresponding authors: pritam.nitjsr@gmail.com & jojin@dtu.dk

Abstract

Zeolitic-imidazolate-frameworks (ZIFs) are crystalline microporous materials that have already shown promising application potential in areas such as gas adsorption and catalysis. Further research advances include studies on integrating ZIFs into nanodevice concepts. In detail for the application e.g. of electron-beam-assisted structural modifications or patterning, there is a need to understand potential structural degradation processes caused by such electron beams.

Advanced transmission electron microscopy (TEM) has demonstrated its ability to study structures at the nanoscale. Here, we systematically investigated electron-beam-induced loss in crystallinity in ZIF-8 under various experimental conditions, using as measure the attenuation of the intensity and the relative displacement of electron diffraction Bragg spots with increasing cumulative electron dose. The intensity and the fading of the {110} Bragg spots indicate the overall stability of the ZIF-8 unit-cell structure, while the {431} Bragg spots are a measure of the stability of ZIF-8's micropore structure. We considered a relative loss of Bragg spot intensity of 37% as the threshold for the critical total electron dose, which was found to be different for different Bragg planes, with 35.6 ± 8.4 $e^{-}Å^{-2}$ for {110} and 11.4 ± 3.0 $e^{-}Å^{-2}$ for {431}. However, the critical dose per breakage of Zn-N bonds in a ZnN_4 tetrahedra per different Bragg plane was found to be ~ 3 $e^{-}Å^{-2}$. This indicates continuous, simultaneous breakage of Zn-N bonds throughout the crystal, confirming radiolysis as the dominant damage mechanism.

In addition, we investigated the effects of TEM experiment parameters, including acceleration voltage, electron dose rate, cryogenic sample temperature, in-situ sample drying, as well as change in conductivity of the sample substrate (e.g., graphene). Our results unravel the degradation mechanisms in ZIF-8 and provide threshold parameters for maximizing resolution in electron-beam-assisted experiments and processes.

1. Introduction

Zeolitic-imidazolate-frameworks (ZIFs) constitute a novel category of microporous materials, demonstrating significant crystallinity within the broader class of metal-organic frameworks (MOFs) [1]. For example, ZIF-8, characterized by a sodalite (SOD) topology, has attracted widespread attention due to its well-defined structure and versatile applications in areas such as gas adsorption, separation, storage, and heterogeneous catalysis [2] [3]. With a framework formula of $[Zn(mim)_2]$ (mim = 2-methylimidazolate) and an I43m space group, ZIF-8 is a typical case of a microporous material with pores of comparably small size (around 1 nm) and a size of the pore's opening aperture of around 3.4 Å [4].

Despite its crystalline nature, MOF crystals inherently exhibit local, non-periodic structural aspects in surfaces and interfaces (i.e. disorder), which play a crucial role in influencing properties related to mass transport through the pores, molecule ad-/de-sorption rates, as well as to catalytic activity and selectivity [5] [6]. For example, the deliberate introduction of defects offers a means to manipulate the structure locally, e.g. its porosity, and generate active open metal sites within MOFs, enabling precise engineering of specific functions [7] [8]. Additionally, guest species, including atoms, few-atom clusters, nanoparticles, and molecules, can accommodate themselves in the ideal frameworks of MOF crystals, giving them stability through heterogenization of the guest species to enhance their properties for particular applications [9] [10] [11] [12] [13].

For example, structure patterning using an electron beam (for example in e-beam lithography, EBL) is a promising approach for designing functional components that include ZIFs in various applications such as sensors, low-k dielectrics, and coatings[14] [15]. The benefits of using an electron beam for patterning ZIFs include high spatial resolution, the ability to create complex patterns, and the overall compatibility with standard micro- and nanofabrication processes. Controlled application of an electron beam enables a controlled local structural rearrangements within the ZIF crystals down to the unit cell level, i.e. controlled manipulation of the long-range order while retaining short-range structure [16], allowing tailor-made patterning of ZIF/MOF materials [14] [15]. However, to understand the structural changes, stability, and amorphization behavior of ZIFs, a detailed knowledge about the underlying mechanism of sequential loss of crystallinity of ZIFs under electron beam irradiation is required. Furthermore, this can contribute to the development of new synthesis methods, improved materials design, and enhanced performance of ZIF-based applications.

Fortunately, such insights can be gained through detailed studies using advanced transmission electron microscopy (TEM). TEM is a very valuable tool for investigating local structures, structural transformations, and MOF stability during the exposure of electron beams on the nanoscale [17] [18] [19]. Recent developments in TEM, such as the flexibility in selecting the appropriate acceleration voltage, the utilization of low electron doses, and observing the material at low sample temperatures, have been pivotal in minimizing the effect of the electron beam on the beam-sensitive MOFs [20] [21]. For example, several low electron dose techniques have been developed, including three-dimensional electron diffraction (3DED) [22], imaging through direct-detection electron-counting (DDEC) cameras [23], and Integrated Differential Phase-Contrast Scanning Transmission Electron Microscopy (iDPC-STEM) [24].

These approaches enable the exploration of MOFs with increased resolution and precision in TEM experiments without structural perturbations. In their study, Zhu et al. preserved the structural integrity of ZIF-8 during the experiment by capturing TEM images on a DDEC camera using an exceptionally low dose of 4.1 $e^{-}Å^{-2}$ [8]. The resulting image conveyed structural details up to 2.1 Å, enabling the resolution of individual atomic columns within the Zn and imidazole linkers of the framework. Notably, they observed that ZIF-8 experiences a rapid loss of crystallinity, transitioning to an amorphous state when the

accumulated dose reaches approximately 25 $e^{-}Å^{-2}$, and complete loss in crystallinity occurs at a cumulative total dose of 75 $e^{-}Å^{-2}$. The assessment of crystallinity loss was based on the fading intensity of Bragg diffraction spots, yet a quantitative measurement correlating the cumulative dose to the extent of crystallinity loss was not provided. However, to understand the relationship between cumulative dose and achievable TEM imaging resolution, a measurement of the cumulative dose up to which the structural integrity is preserved, known as critical dose, should be measured for various lattice (Bragg) planes.

Li et al. used cryogenic electron microscopy (cryo-EM) to stabilize the structure and resolved the atomic surface of ZIF-8 and investigated its interaction with guest CO_2 molecules [25]. They observed that ZIF-8 becomes amorphized at an accumulated dose of around 50 $e^{-}Å^{-2}$ at room temperature when using an acceleration voltage of 300 keV. The sample, when kept at -170 °C during the cryo-EM experiment, showed partial loss of crystallinity at a cumulative dose of 90 $e^{-}Å^{-2}$, determined by measuring the fading of normalized intensity of spots in the fast Fourier transform (FFT) pattern obtained from HRTEM images. They reported that imaging ZIF-8 under cryo temperature at 300 keV improves the damage tolerance by a factor of two, as compared to imaging at room temperature. The effect of cryo temperature at lower accelerating voltage on the damage tolerance and the critical dose is still unexplored.

Patterson et al. used liquid cell TEM (LC-TEM) to understand the self-assembly and growth of ZIF-8 under different synthetic conditions and its effects on particle size [26]. The relationship between dynamics of particle growth of ZIF-8 was established with synthetic conditions at different electron dose rate and total accumulated dose, as well as at different accelerating voltages. Therefore, it is also important to investigate the accelerating voltage's effect on the measured critical dose and the electron dose rate in $e^{-}Å^{-2}\ s^{-1}$, i.e. how many electrons interact with ZIF-8 per Angstrom area in 1 sec. Further, in the quantitative and accurate measurement of critical dose it is very important to distinguish between dose dependent crystal damage vs structural changes introduced due to external stimuli during in-situ TEM experiments such as temperature.

Jain et al. explored the influence of cryogenic temperatures, accelerating voltage, graphene as the TEM substrate material and studied their effects on prolonging the lifetime of the PbPc crystal structure during the TEM investigation[27]. Since ZIF-8 is non-conducting, using conducting substrate, such as graphene, could potentially reduce the sample charging effect during TEM imaging. The effect of conducting substrate on the critical dose for ZIF-8 has not been studied so far.

The electron beam-induced degradation of ZIF-L, another ZIF structure, was studied using fading of Bragg spot intensities in electron diffraction (ED) pattern as well as shifts in bond energies using electron energy loss spectroscopy (EELS). They reported a two-stage degradation process when exposed to the electron beam: a structural damage up to a full amorphization of ZIF-L, and, second, a molecular breakdown of the organic 2-methylimidazole linker[28]. The mechanism of damage of unit cell and the loss of crystallinity during the first stage of structural damage has not been studied further.

Here, we systematically investigated the effect of electron beam exposure under various experimental conditions on the crystallinity state of ZIF-8, using as quantitative measure the attenuation (i.e. fading) of the intensity and the relative displacement of ED Bragg spots with increasing cumulative electron dose. Bragg spots corresponding to low index planes such as {110}, {211}, {220} and {200} as well as high index planes such as {400} and {431} are used as indicators of the stability of structural features in ZIF-8 crystals (e.g. of ZnN_4 tetrahedra). For example, the intensity and the fading of the {110} Bragg spots in the ED pattern provide information about the stability of the overall ZIF-8 unit-cell structure, while the continuous presence of {431} Bragg spots indicates that ZIF-8's pore aperture is still intact.

The measurement of the critical electron doses for such intensity fading and for relative displacement of different crystal planes provides insights about the sequential loss in ZIF-8's crystallinity as a function of

critical cumulated electron dose and allows to elucidate the underlying damage mechanism. The individual critical doses for all of the above-mentioned Bragg planes were quantitatively determined at the point where the Bragg spot lost 37 % in intensity, which interestingly coincides with the observed relative displacement of Bragg planes by 37% [27] [29] [30].

It is significant to quantify the critical electron dose limit specifically for the {431} Bragg planes, as this is a measure of the limit in electron beam exposure up to which the pore structure remains intact. And this directly affects ZIF-8's applications, as the interconnected gates with definite aperture size play a crucial role in gas adsorption[31] and gas separation[32].

We investigated the effects of TEM experiment parameters, including acceleration voltage, electron dose rate, as well as change in conductivity of the sample substrate (e.g., using graphene) as protective measures to further elucidate on their effects on the damage caused by the electron beam. Further, the effect of temperature was investigated, such as cryo temperature and sample drying at 125°C in vacuum.

The effect of the critical cumulative dose obtained from the ED studies were confirmed in a high-resolution TEM (HRTEM) experiment showing lattice fringes in an HRTEM image of a ZIF-8 particle.

2. Materials and Methods

2.1. ZIF-8 synthesis:

ZIF-8 MOF was synthesized using wet chemical synthesis method mentioned elsewhere [13]. A solution containing 775 mg of 2-methylimidazole (9.44 mmol) dissolved in 10 mL of methanol (MeOH) was mixed with a solution of 350 mg of $Zn(NO_3)_2 \cdot 4H_2O$ (1.34 mmol) in 10 mL of MeOH at 50 °C. The resulting suspension was stirred for 5 minutes and aged for 10 minutes. The suspension was then centrifuged, washed with tetrahydrofuran (THF) (3×10 mL), and then dried in vacuum. The final product was a white powder with a weight of 66 mg.

2.2. TEM sample preparation:

For TEM sample preparation, 1mg of quantity of ZIF-8 powder was dispersed in 2ml of ethanol solution (70 wt.%) and ultrasonicated for 30 mins to obtain a colloidal solution. The solution was dropcasted on holey carbon (AGS147) and graphene coated Cu grid purchased from Agar Scientific (AGS179-GO4, suspended monolayer Graphene on TEM grid Quantifoil R2/4).

2.3 Electron Diffraction experiment:

The electron diffraction (ED) experiments at 300 keV were performed using a ThermoFisher Titan microscope equipped with a field emission gun. The microscope was operated in spot size 3 and the dose rate was tuned by adjusting the electron beam current using monochromator focus (gun lens) while keeping the exposure time and the illuminated sample area constant. The beam current was measured by capturing an image without the sample (vacuum) using a Gatan OneView camera with exposure time of 1 sec and then determining the average number of electrons per pixel. The dose rates were calculated by dividing beam currents by area of a pixel. Different dose rates such as 0.33, 0.5, 1 and 2 $e^{-}Å^{-2}s^{-1}$ were used for the experiment as shown in Table 1. The screening of the TEM sample to locate the ZIF-8 particles was done in imaging mode at 10000x magnification with an exposure time of 40 µsec. The particle size is in the range of 150 nm to 230 nm with an average size of 180 nm. ZIF-8 has a cubic crystal structure (space group I43m, lattice parameter = 16.99Å) with large pores of 11.6 Å. The particles are homogeneously distributed with minimal overlap. As soon as the particles were observed, the beam was blanked, and the microscope was

switched to diffraction mode. The exposure time and camera length were set to 1 sec and 1.5 mm, respectively. The series of ED patterns were recorded at a constant dose rate until all the Bragg rings disappeared. All the experiments were repeated three times for better statistics. The ED patterns were recorded in 2k x 2k size with pixel size of 0.0069 1/nm.

The diffraction experiment at 200 keV was performed using a ThermoFisher Tecnai G2 microscope with LaB_6 gun. The microscope was operated in spot size 9 keeping the exposure time of 1 sec and beam diameter of 2µm constant. The beam current was measured using screen readout calibrated using a Faraday cup. The dose rates of 1 $e^{-}Å^{-2}s^{-1}$, used for the experiment, were calculated by dividing beam current of 0.050 nA with an area of a beam with radius of 1µm. The sample screening was done in imaging mode at 11000x magnification with an exposure time of 40 µsec. As soon as the ZIF-8 particles were in the field of view, the beam was blank, and the microscope was switched to diffraction mode. The exposure time and camera length were set to 1 sec and 1.5 mm, respectively. The series of ED patterns were recorded using a TVIPS camera at a constant dose rate until all the Bragg rings disappeared. All the experiments were repeated three times for better statistics. The diffraction patterns were recorded in 768 x 768 size with pixel size of 0.024 1/nm.

2.4. HRTEM imaging: The HRTEM imaging was performed at 300 keV using a ThermoFisher Titan microscope with field emission gun and monochromator. The search for the best sample area was done in real space at a dose rate of 0.01 $e^{-}Å^{-2}s^{-1}$ at 5000X. A well faceted ZIF-8 particle with hexagonal shape, presuming oriented along [111] zone axis, was selected for HRTEM imaging. Magnification was increased to 87000X, the ZIF-8 particle was imaged with an approx. electron dose rate of 0.5 $e^{-}Å^{-2}s^{-1}$. The beam was blanked at any intermediate stage. At last, the magnification was increased to 145 kX, the HRTEM was acquired at a dose rate of 5.2 $e^{-}Å^{-2}s^{-1}$ with an exposure time of 3 seconds. The total cumulative dose of the HRTEM imaging was around 19 $e^{-}Å^{-2}$. The power spectrum is calculated from the modulus of the complex Fast Fourier Transform (FFT) from the HRTEM image.

2.5. Cryo experiment: The ZIF-8 particles were drop casted on a Cu TEM grid and then loaded on a Gatan 626 cryo holder at room temperature. Cryo TEM experiments were done using a ThermoFisher Tecnai microscope operated at 200 keV and a ThermoFisher TITAN operated at 300 keV respectively. After inserting the holder into the microscope, the sample was cooled down to -176 ºC using liquid N_2. After waiting for 30 mins to stabilize the temperature, the ED series acquisition process is the same as described in the diffraction experiment. The dose rate and exposure time were kept constant at 1 $e^{-}Å^{-2}s^{-1}$ and 1 sec respectively for both experiments.

2.6. Heating experiment: The ZIF-8 particles were drop-casted on a Cu TEM grid with holey amorphous carbon support. The heating experiment was performed in a ThermoFisher Titan microscope operated at 300 keV using a Gatan INCONEL heating holder. The sample was heated from room temperature to 125°C at a heating rate of 1 °C per sec and then the temperature was held for 1 hour. Then the diffraction series acquisition was carried out. Later, the sample was cooled down to room temperature and again diffraction series acquisition was done. The dose rate and exposure time were kept constant at 1 $e^{-}Å^{-2}s^{-1}$ and 1 sec, respectively, in both experiments.

2.7. Data analysis:

The indexing of Bragg rings in the electron diffraction pattern of ZIF-8 was done using Gatan Digital Micrograph GMS 3.5 software. The measurement of radial averaging of intensity of Bragg planes was done using a MATLAB script. To measure the relative peak intensities of the Bragg planes in the series, the last diffraction pattern of the series (i.e. with no Bragg spots present anymore) was used as the background for all diffraction patterns in the series. To obtain the peak intensities of the Bragg planes of the first diffraction

pattern, as shown in fig. 1(f), the intensities in the last diffraction pattern were considered as the background (i.e. the red curve was subtracted from the blue curve). The same process was applied to all the diffraction patterns as a function of cumulative dose, while keeping the dose rate constant. The maximum radial average intensity of selected Bragg planes and their position in reciprocal space were measured vs. cumulative dose. The fading of relative intensity of Bragg planes were measured to estimate the critical dose. Also, the expansion in the diameter of the Bragg rings in reciprocal space with cumulative dose (i.e. the shrinkage in the Bragg planes in real space) was measured. The mean and standard deviation of the critical dose are calculated from three different diffraction experiments.

3. Results:

Fig. 1(a) shows the low magnification 300 kV TEM image of multiple ZIF-8 particles supported on holey amorphous carbon using low dose rate condition of 1 $e^{-}Å^{-2}s^{-1}$. The particle size is in the range of 150 nm to 230 nm, with an average size of 180 nm. The left inset in fig. 1(a) shows the HRTEM image of single ZIF-8 particle acquired at a dose rate of ca. 5.2 $e^{-}Å^{-2}s^{-1}$, with an exposure time of 3 sec and a total accumulated dose of around 19 $e^{-}Å^{-2}$. The right inset in fig. 1(a) shows the power spectrum from the ZIF-8 particle, oriented along [111] direction. The {110} and {211} Bragg spots are resolved. Fig. 1(b) shows the ring electron diffraction (ED) pattern of several ZIF-8 particles recorded with electron dose rate of 1 $e^{-}Å^{-2}s^{-1}$ and an exposure time of 1 sec. Details about estimating the applied electron dose rate is described in the *Methods* section. The highest spatial frequency obtained from the diffraction pattern is 7 nm^{-1} marked with green circle in fig. 1(b), which corresponds to a spatial resolution of ~1.4 Å. The Bragg planes with increasing spatial frequency are marked with red dotted circles in fig. 1(b) as follows: {110}, {200}, {211}, {222}, {400}, and {431}.

We have also observed the same trend in the loss of crystallinity of ZIF-8 as reported in [8], from the fading of intensity of Bragg rings, as shown in fig. S1(a-c).

ZIF-8 has a cubic crystal structure (space group I43m, lattice parameter = 16.99Å) with large pores of 11.6 Å, the perspective view and top view along {111} direction is shown in fig. 1(c) and 1(d) respectively. The location of the Bragg planes (that are marked with red circles in fig. 1(b)) are indicated in the model of a ZIF-8 unit cell in fig. 1(c) and 1(d), respectively. The pores in the unit cell are interconnected using the gates with aperture size of 3.4 Å shown (with a yellow circle) in fig. 1(d), which is represented by {431} planes, shown by the larges red circle in the ED pattern in fig. 1(b).

The radial averaging of the intensity of the Bragg planes is plotted in fig. 1(e) as a function of spatial frequency measured from the center of the diffraction pattern. Blue and red curves represent the average radial intensity profile of the first and last diffraction pattern, respectively. The first diffraction pattern (blue curve) exhibits the average intensities of the Bragg rings due to elastic scattering whereas the last diffraction pattern (red curve) shows the average intensities of the background caused by inelastic electron scattering on the now fully amorphous ZIF-8. The subtracted radial intensity profile of the first and second last diffraction pattern is shown in fig. 1(f), which signifies that a complete loss of crystallinity has occurred at the end of the diffraction pattern time series.

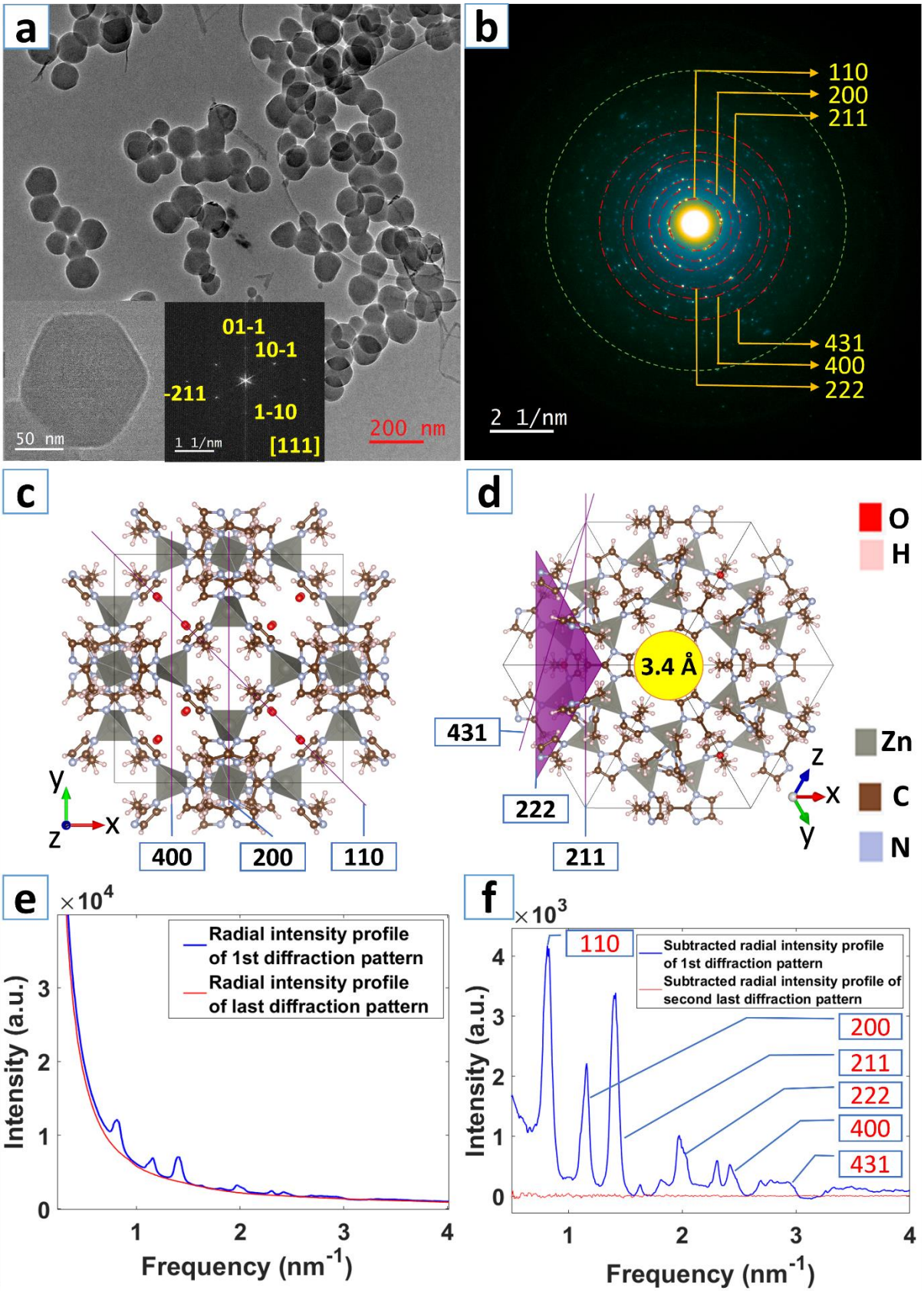

Fig. 1. (a) low magnification phase contrast TEM image of the ZIF-8, supported on holey amorphous carbon, at 300 keV (inset, left: HRTEM lattice image of ZIF-8 particle; inset, right: power spectrum from the lattice image along [111] zone axis). (b) electron diffraction (ED) pattern of several ZIF-8 particles (at an electron dose rate of 1 $e^{-}Å^{-2}s^{-1}$) showing the Bragg planes with red rings. (c, d) Crystal structure of ZIF-8 generated using VESTA software [33] *showing perspective view and along [111] direction respectively. The Bragg planes such as {110}, {200}, {400}, {211}, {222} and {431} are shown in fig. 1(c) and 1(d) respectively. The pore aperture of 3.4 Å is shown with yellow circle in fig. 1(d). (e) Plot showing radial averaging of the intensity of Bragg planes as a function of spatial frequency from the center of the diffraction pattern of first and last diffraction pattern of the series. (f) Plot showing the subtracted radial intensity profile of first and second last diffraction pattern with marked Bragg planes.*

The critical dose is now measured by analyzing the amount of fading of the subtracted peak intensity of the Bragg rings as a function of cumulative dose. It is reported in literature that a cumulative dose is considered as the critical dose when the relative intensity of the Bragg ring decreased by 1/e (i.e. by 37 %) [27] [29] [30]. The peak maxima of {110} and {431} Bragg rings are measured and relative intensities of the {110} Bragg rings are plotted as a function of cumulative dose in fig. S1(d). Along with the fading of the relative intensity, it was noticed that the radius of the Bragg rings also increases with increasing cumulative dose, which is observed by the outward shift of the position of the peak maxima on a linear scale as shown in fig S1. The displacement in the reciprocal lattice parameters of different Bragg planes such as {110}, {200}, {211}, {222} and {431} as a function of cumulative dose is shown in fig. S1(e-i) respectively. This increase in spatial frequency is a measure of the shrinkage in the lattice spacing in real space. The initial and final real-space lattice parameter of {110} Bragg plane is measured as 12.2 Å and 11.0 Å respectively, and the total lattice plane shrinkage is measured as 1.2 Å, as shown in fig. S1(d). Relative displacement as a function of cumulative dose is measured as the ratio of displacement of Bragg plane at certain accumulated dose and total displacement. The relative intensity and relative displacement of {110} Bragg ring as function of cumulative dose is plotted in fig. 2(a) using a blue and a red curve, respectively.

The critical dose for the {110} Bragg plane is considered when the relative {110} intensity drops by 1/e (37 %). Therefore, the critical dose for the {110} in ZIF-8 is around 35 $e^{-}Å^{-2}$, as marked by a blue line in fig. 2(a).

As mentioned, we observed a simultaneous shrinkage in the ZIF-8 unit cell size. The lattice parameter of {110} Bragg plane at the beginning of the experiment was 12.20 ± 0.07 Å. As the cumulative dose increases, the lattice parameter of {110} Bragg plane starts decreasing and reaches the final value of 11.00 ± 0.12 Å. The total shrinkage in the {110} Bragg plane was 1.25 ± 0.14 Å.

Interestingly, when we now consider the critical dose for {110} Bragg plane as the cumulative dose at which the Bragg plane is simultaneously displaced relatively by 1/e (a shrinkage by 37%), then the critical dose for the {110} in ZIF-8 is around 33 $e^{-}Å^{-2}$, marked by red line. The 37 % shrinkage at the critical dose was measured with 0.41 ± 0.05 Å. This indicates that the ZIF-8 is considered to maintain crystallinity if the shrinkage in 110 Bragg plane is less than 0.4 Å.

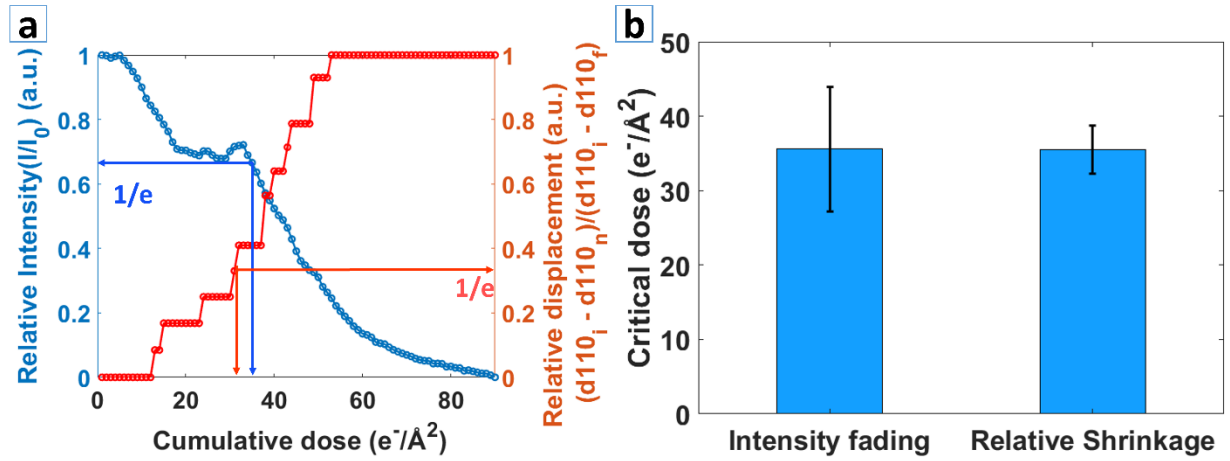

Fig. 2 (a) Fading of relative intensity and relative displacement of {110} Bragg plane with cumulative dose; blue and red arrow shows the (1/e) times relative intensity and relative displacement of {110} Bragg plane respectively, measured as critical dose. (b) Comparison of measured critical dose from fading of relative intensity and relative displacement respectively.

Statistical analysis in fig. 2(b) shows that the critical dose calculated from the Bragg spot's fading intensity and the lattice plane's relative displacement in fact coincide, within the limits of standard deviations.

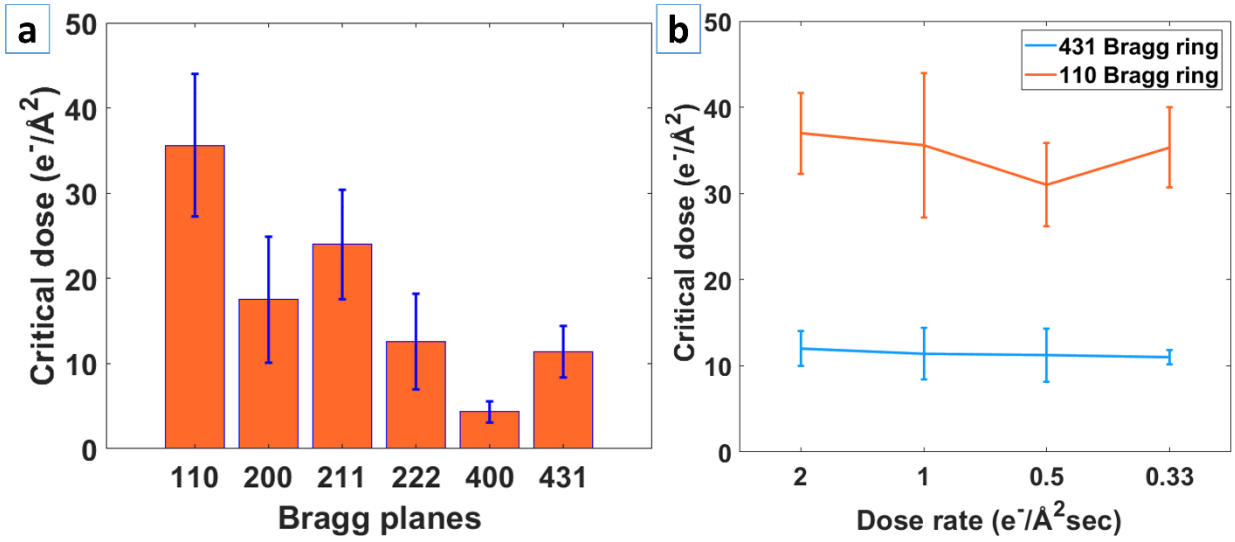

Fig. 3 (a) Bar plot showing measured critical dose of different Bragg planes in ZIF-8 from low-index planes to high-index planes at dose rate of 1 $e^{-}Å^{-2}s^{-1}$ (at 300 keV). (b) Comparison of critical dose of {110} and {431} Bragg planes with varying dose rates.

Fig. 3(a) shows the measured critical dose for different Bragg planes, from low-index planes to high-index planes, at an electron dose rate of 1 $e^{-}Å^{-2}s^{-1}$ and an accelerating voltage of 300 keV. It indicates that the critical dose of high index planes, such as {400}, {431} etc., is lower compared to the critical dose of low index planes, such as {110}, {200}, {211} and {222} etc.

The critical dose of {431} Bragg plane is 11.4 ± 3.0 $e^{-}Å^{-2}$ as the threshold up to which the ZIF-8 pore aperture stays intact. In HRTEM imaging beyond this critical dose, the crystalline porous structure cannot be resolved. As an example, the phase-contrast TEM image of ZIF-8 in fig 1(a) (left inset) was acquired with cumulative dose larger than 11 $e^{-}Å^{-2}$, hence, the {431} Bragg plane is already affected by the electron beam and is therefore absent in the corresponding FFT pattern. Detailed analyses show that the critical dose for {400} Bragg plane is 4.0 ± 1.2 $e^{-}Å^{-2}$. The {222} Bragg plane, which represents half of the body diagonal of the cubic ZIF-8 (see fig 1c, d), collapses when the critical dose exceeds 12.6 ± 5.6 $e^{-}Å^{-2}$. The {200} Bragg plane collapses as the critical dose exceeds 17.5 ± 7.4 $e^{-}Å^{-2}$, followed by the {211} Bragg plane with a critical dose of 24.0 ± 6.4 $e^{-}Å^{-2}$. At last, the {110} Bragg plane loses its crystallinity beyond the critical dose of 35.6 ± 8.4 $e^{-}Å^{-2}$.

Table 1: Calculation of varying dose rates.

S. No	Average (e^{-}/pixel)	Std dev (e^{-}/pixel)	Pixel size (Å)	Exposure time (sec)	Area of pixel ($Å^2$)	Dose rate ($e^{-}Å^{-2}s^{-1}$)
1.	956.873	21.95	22.23	1	494.17	1.93±0.04
2.	568.087	16.64	22.23	1	494.17	1.08±0.03
3.	245.017	11.05	22.23	1	494.17	0.49±0.02
4.	163.75	9.34	22.23	1	494.17	0.33±0.02

Further, the effect of the electron dose rate on the critical dose of the ZIF-8 has been investigated.

The TEM images of the electron beam in the vacuum region with varying beam current and corresponding line profiles of electron counts are shown in fig. S2(a-d) and S2(e-h), respectively. The average electron counts per pixel, pixel size and exposure time required for calculation of dose rates are given in table 1. Fig. S3(a-d) shows the diffraction patterns of ZIF-8 acquired at different electron dose rates of 2, 1, 0.5 and 0.3 $e^{-}Å^{-2}s^{-1}$, respectively, recorded with an exposure time of 1 sec.

Further, in Fig. S4(a-c) the fading of relative intensity and the relative displacement of {110} Bragg plane as a function of cumulative dose is plotted for varying dose rates of 2.0, 0.5 and 0.33 $e^{-}Å^{-2}s^{-1}$, respectively. The results of varying electron dose rate (0.33, 0.5, 1.0, and 2.0 $e^{-}Å^{-2}s^{-1}$ on the critical dose of {110} and {431} Bragg plane is plotted in fig. 3(b). Interestingly, the critical dose for the {110} and the {431} Bragg plane do not change significantly when varying the electron dose rate between 0.33 and 2.0 $e^{-}Å^{-2}s^{-1}$.

In fig. 4, the effect of further experimental TEM parameters on the loss of crystallinity or critical dose is presented, such as incident electron energy (i.e. acceleration voltage), of the choice of TEM substrate material and sample temperature. Fig. 4(a) shows the effect of reducing the accelerating voltage from 300 kV to 200kV and of changing the substrate material from holey carbon to conductive graphene (see Methods for details) on the critical dose of {110} and {431} Bragg plane at fixed dose rate of 1 $e^{-}Å^{-2}s^{-1}$. A low magnification TEM image and ED pattern of the ZIF-8 particles supported on holey carbon are shown in fig. S5(a) and S5(b), respectively.

While there is only a slight decrease in the critical dose of {431} Bragg plane from 11.4 ± 3.0 $e^{-}Å^{-2}$ to 8.7 ± 1.2 $e^{-}Å^{-2}$ when lowering accelerating voltage from 300 keV to 200 keV, whereas the decrease in the critical dose of the {110} plane is more severe from 35.6 ± 8.4 $e^{-}Å^{-2}$ to 12.7 ± 3.3 $e^{-}Å^{-2}$. For comparison, the fading of relative intensities of {431} and {110} Bragg rings at 200 keV is shown in fig. S5(c). Note:

The local peak maxima in the relative intensities of Bragg rings are results of particle reorientation during the exposure of electron beam at room temperature (RT) [34] [35] as well as at cryo-temperature [36] [37].

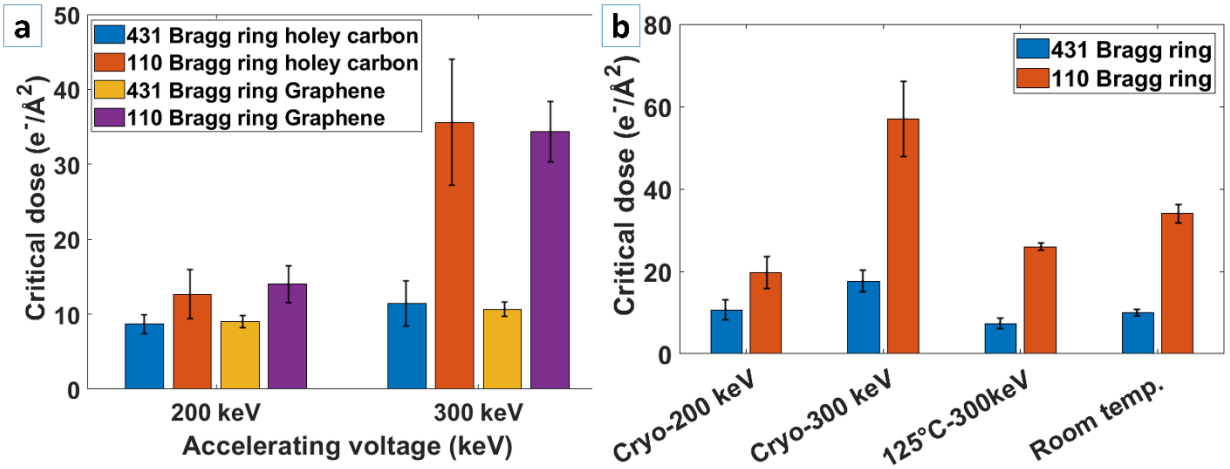

Fig. 4(a) Comparison of varying accelerating voltage on the critical dose of 110 and 431 Bragg plane of ZIF-8 at dose rate of 1 $e^{-}Å^{-2}s^{-1}$. (b) Bar plot showing effect of conducting substrate and cryogenic temperature on the loss of crystallinity of 110 and 431 Bragg plane of ZIF-8 at 200 keV with dose rate of 1 $e^{-}Å^{-2}s^{-1}$.

To investigate the effect of the choice of the material to support ZIF-8 on the TEM grid (= substrate), the material was change from the standard holey carbon to single layer graphene with a better electron conductivity [27].

Fig. 4(a) shows the effect of switching to graphene as substrate on the loss of crystallinity of {110} and {431} Bragg plane of ZIF-8, at 200 keV and at 300 keV with a constant dose rate of 1 $e^{-}Å^{-2}s^{-1}$. There is no significant effect on the critical dose of different planes when using graphene as TEM substrate material. In detail, a low magnification TEM image of ZIF-8 on graphene and the corresponding diffraction patterns are shown in fig. S6(a, b). Fig. S6(c, d) shows the diffraction patterns of ZIF-8 supported on graphene substrate at 300 and 200 keV, respectively. Fig. S6(e, f) shows the fading of relative intensity of {431} and {110} Bragg rings at 300 and 200 keV, respectively.

At last, we examined the effect of the TEM sample temperature on the critical dose tolerance limit of ZIF-8. The ZIF-8 is cooled down to cryogenic temperature and the critical dose of {431} and {110} Bragg planes are measured at 200 and 300 keV as shown in fig. 4(b). Fig. S7 (a, b) show the diffraction patterns of ZIF-8 cooled down to cryo temperature at 300 and 200 keV, respectively. Fading of relative intensity of {431} and {110} Bragg ring at 300 and 200 keV, respectively, under cryo temperature is shown in fig. S7(c, d). The critical dose of {431} and {110} Bragg planes at 200 keV were determined as 10.7 ± 2.5 $e^{-}Å^{-2}$ and 19.7 ± 3.8 $e^{-}Å^{-2}$, respectively, which increased at 300 keV to 17.7 ± 2.6 $e^{-}Å^{-2}$ and 57.0 ± 9.2 $e^{-}Å^{-2}$, respectively.

We also investigated if there is an effect of any potential presence of a residual volatile substance in the pores of ZIF-8, e.g. water/moisture or other solvents, which might cause additional interaction with the electron beam. To evaporate such substances in the TEM vacuum, the ZIF-8 sample was heated in the TEM to 125°C for 1 hour using an in-situ heating holder and subsequently cooled down back to RT. Fig. S8 (a, b) show diffraction patterns of ZIF-8 at 300 keV at 125°C and after it has been cooled down to RT, respectively. In fig. S8 (c, d), the fading of relative intensity of {431} and {110} Bragg ring, at 125°C and

at RT, is plotted. The critical dose of {431} and {110} Bragg plane at 125°C was measured as 7.3 ± 1.2 $e^{-}Å^{-2}$ and 26.0 ± 0.8 $e^{-}Å^{-2}$, respectively, and plotted in fig. 4(b). After cooling down to RT, the critical dose for {431} and {110} Bragg plane was again around 10.0 ± 0.8 $e^{-}Å^{-2}$ and 34.0 ± 2.2 $e^{-}Å^{-2}$, respectively, close to the values at RT measurements (fig. 1).

Table 2: Critical dose of {431} and {110} Bragg plane under different conditions.

S. No	Substrate	Dose rate ($e^{-}Å^{-2}s^{-1}$)	Accelerating voltage (keV)	Temperature (°C)	Critical dose 431 Bragg plane ($e^{-}Å^{-2}$)	Critical dose 110 Bragg plane ($e^{-}Å^{-2}$)
1.	Holey carbon	1	200	RT	8.66 ± 1.24	12.66 ± 3.29
2.	Graphene	1	200	RT	9 ± 0.81	14 ± 2.44
3.	Graphene	1	200	-176	10.66 ± 2.49	19.66 ± 3.85
4.	Holey carbon	1	300	RT	11.4 ± 3	35.6 ± 8.38
5.	Holey carbon	2	300	RT	12 ± 2	37 ± 4.71
6.	Holey carbon	0.5	300	RT	11.25 ± 3.11	31 ± 4.84
7.	Holey carbon	0.33	300	RT	11 ± 0.81	35.33 ± 4.64
8.	Graphene	1	300	RT	10.66 ± 0.94	34.33 ± 4.027
9.	Holey carbon	1	300	-176	17.66 ± 2.62	57 ± 9.20
10.	Holey carbon	1	300	125	7.33 ± 1.24	26 ± 0.81
11.	Holey carbon	1	300	Cooled to RT	10 ± 0.81	34 ± 2.16

Table 2 summarizes the values of calculated critical doses of {431} and {110} Bragg planes when varying the electron dose rate, the substrate material, as well as the sample temperature.

Discussion:

To decode the mechanism of loss of crystallinity of ZIF-8 due to electron beam irradiation, we first need to understand the structure of ZIF-8 crystal itself. The fundamental building block of ZIF-8 comprises a single zinc atom linked with four imidazolate units, forming a tetrahedral structure. This arrangement, characterized by N–Zn bonds and N–Zn–N angles, embodies a composite framework integrating organic and inorganic components. The N-Zn bond is considered as weakest in ZIF-8 structure[38][39], which has the bond dissociation enthalpy of 353 $KJmol^{-1}$[40]. Utilizing the flexible ZnN_4 tetrahedra, a conceptual model featuring two fully adaptable gates emerges, including a 4-membered ring (4MR) and a 6-membered ring (6MR). Notably, the 6MR gate, with size of 3.4 Å, acts as the primary entry point for guest molecules, facilitating their transfer between adjacent cavities[41]. The 6MR gate or aperture size is represented by {431} Bragg plane.

As the ZIF-8 crystal is exposed to the electron beam, the fading of intensity and displacement of Bragg planes indicates that the electron beam affects the structural integrity. The fading of intensity of Bragg plane indicates defect formation and bond breaking in the crystal, whereas the displacement in the Bragg plane

signifies volume shrinkage. The results of fig. 3(a) indicate that the high index planes (such as 400 and 431) fade faster as compared to low index planes (such as 110, 211 and 222). Fig. 5 also shows the relative displacement of different Bragg planes indicating that high index planes collapse first as compared to low index planes (at 300 keV).

We have divided the loss of crystallinity of ZIF-8 into several steps depending upon the sequence of collapse of different Bragg planes. The left inset within the relative displacement vs cumulative dose plot in fig. 5. shows the pristine ZIF-8 unit-cell viewed along [110] directions featuring 4MR and 6MR.

In step I, the relative intensity of {431} starts fading as shown in fig. S1(c) but there is no relative displacement observed up to a cumulative electron dose of 9 $e^{-}Å^{-2}$. The N-Zn bonds start breaking, leading to the formation of several point defects such as dangling linker (DL) and linker vacancy (LV) defects[42][43]. When the cumulative dose is below 9 $e^{-}Å^{-2}$, point defect density is low as well, and no lattice displacement has been observed. It is safe to assume that crystallinity is still intact, with just a few point defects present (as indicated with red lightening shape in Fig 5).

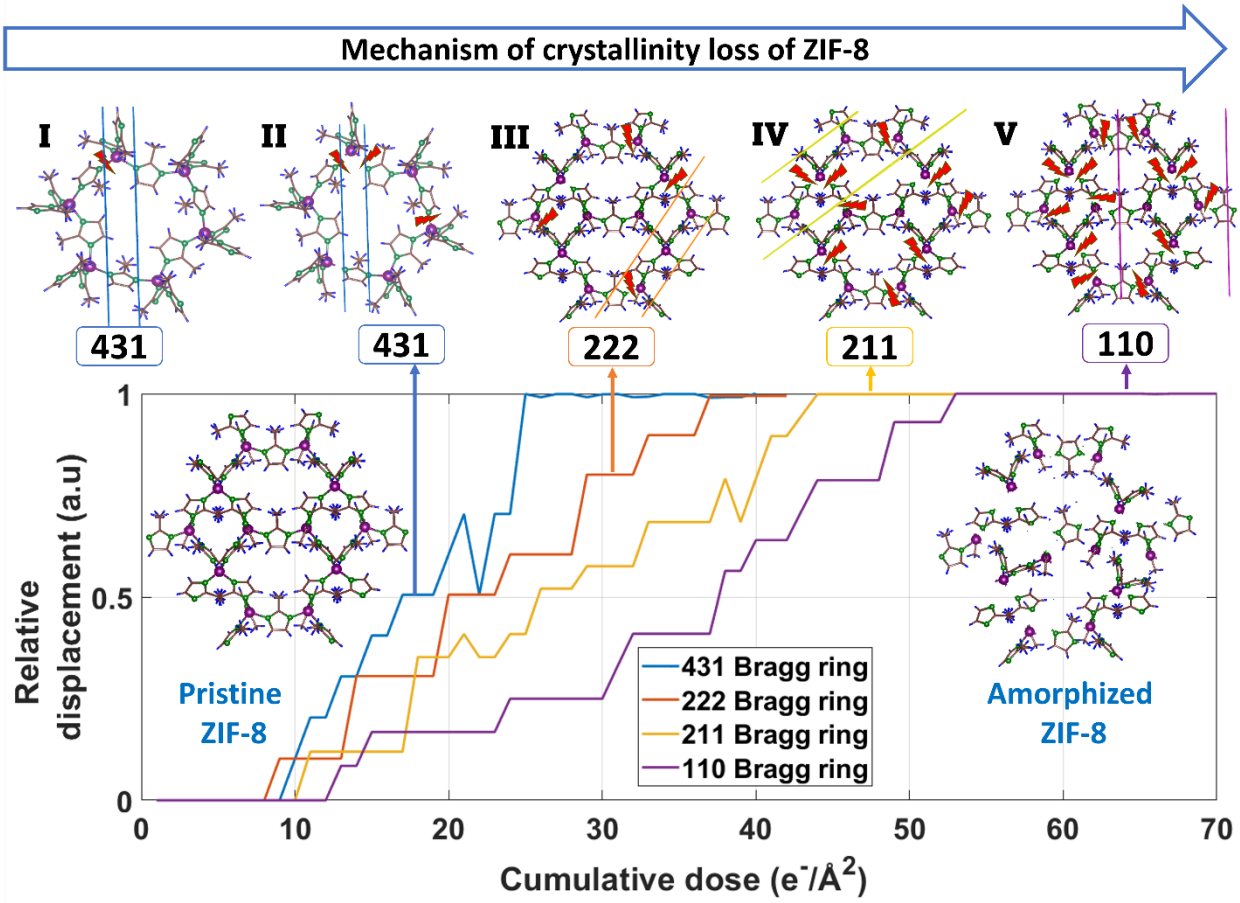

Fig. 5 Schematic representing the step-by-step (step I to step VI) of loss in crystallinity of ZIF-8 with increasing cumulative dose.

In step II, the increasing number of introduced point defects begins to lead to the formation of clusters of defects, such as defect-pairs or defect-triplets. First principal calculations have shown that the defect-triplet has lower formation energy as compared to defect-pairs[44]. The {431} Bragg planes, marked with blue lines in 6MR ring, start shrinking as the cumulative dose increases beyond 9 $e^{-}Å^{-2}$ and completely collapse

as the cumulative dose reaches a value of 25 $e^{-}Å^{-2}$. The formation of defect cluster surrounding the ZnN_4 tetrahedra causes the displacement of ZnN_4 tetrahedra, leading to the shrinkage in the {431} planes. The total displacement of {431} planes was 0.1 Å before it completely collapsed, as shown in fig. S1(i), and the rate of change in relative displacement per unit dose was 0.047 ($1/e^{-}Å^{-2}s^{-1}$) as measured from fig. S9(a), presented in table 3.

In step III, as the 6MR gate or the aperture has collapsed, the displacement of {222} plane is still in progress. Displacement in {222} plane signifies the change in the interplanar spacing of ABC stacking along the body diagonal of the ZIF-8 unit cell. Each stacking contains 6 ZnN_4 tetrahedra per unit cell as compared to 3 ZnN_4 tetrahedra in {431} planes. Therefore, a higher cumulative dose is required to break all these N-Zn bonds. As the cumulative dose exceeds 35 $e^{-}Å^{-2}$, the {222} plane has completely collapsed. The total displacement of {222} planes, before it completely collapsed, was 0.2 Å, as shown in fig. S1(h), and the rate of change in relative displacement per unit dose was 0.033 ($1/e^{-}Å^{-2}s^{-1}$) as measured from fig. S9(b), presented in table 3.

In step IV, the {211} plane collapses, which holds the 4MR with the 6MR. First principle calculations suggest that the formation of defect-triplet is more favorable in 6MR, whereas defect-pair formation are preferred in 4MR. There are 8 ZnN_4 tetrahedra present in each {211} planes per unit cell, which is more then they are present in the {222} plane. Therefore, {211} planes undergo total displacement of 0.6 Å before collapse at cumulative dose greater than 45 $e^{-}Å^{-2}$, as shown in fig. S1(g). The rate of change in relative displacement per unit dose was 0.026 ($1/e^{-}Å^{-2}s^{-1}$) as measured from fig. S9(c), presented in table 3. In step V, the 3D network or structure of the pore cavity, represented by the {110} planes, fully collapses. It contains 12 ZnN_4 tetrahedra, which requires significantly higher cumulative dose as compared to other planes. The total displacement of {110} planes before it collapsed was 1.2 Å, as shown in fig. S1(e), and the rate of change in relative displacement per unit dose was 0.023 ($1/e^{-}Å^{-2}s^{-1}$) as measured from fig. S9(d). Beyond a cumulative dose of 55 $e^{-}Å^{-2}$, the amorphization of the ZIF-8 particle takes place. The bonds present in the imidazolate linker are stronger than the N-Zn bonds, therefore the imidazole units remains unaltered during the loss of crystallization process[28][40]. The sequence of loss of crystallinity of Bragg planes calculated from the rates of relative displacement in fig. S9 matches well with the fading of relative intensity of Bragg planes in fig. 3(a).

Step No.	Bragg Plane	No. of ZnN_4 tetrahedra	Total displacement (Å)	Relative displacement per unit electron dose ($1/e^{-}Å^{-2}s^{-1}$)	Critical dose ($e^{-}Å^{-2}s^{-1}$)	Critical dose per ZnN_4 tetrahedra ($e^{-}Å^{-2}s^{-1}$)
II	431	3	0.1	0.047	11.4 ± 3.0	3.0 ± 0.9
III	222	6	0.2	0.033	12.6 ± 5.6	2.1 ± 0.9
IV	211	8	0.6	0.026	24.0 ± 6.4	3.0 ± 0.8
V	110	12	1.2	0.023	35.6 ± 8.4	3.0 ± 0.7

Table 3: Comparison of critical dose per ZnN_4 tetrahedra and relative displacement per unit electron dose of different Bragg planes.

Comparing the critical dose and relative displacement of different Bragg planes (see Table 3) suggests that the critical dose required to break the Zn-N bonds in a ZnN_4 tetrahedra is almost the same for all the Bragg planes, namely about 3.0 ± 0.9 $e^{-}Å^{-2}$, which means the breaking of Zn-N bonds occurs simultaneously throughout the crystal under the influence of an electron beam. Bragg rings of high index planes such as {431} fade and shrink in the beginning due to a smaller number of ZnN_4 tetrahedra, whereas Bragg rings

of low index planes such as {110}, {211} and {222} with a higher number of ZnN_4 tetrahedra fade slower. This degradation behavior of the crystal justifies the radiolysis damage mechanism [45].

The resolution achievable in HRTEM imaging of the ZIF-8 depends upon the total dose used in the experiment, and therefore the critical dose has a significant effect on the achievable resolution. If the cumulative dose is below 7 $e^{-}Å^{-2}$, high frequency planes can be resolved with achievable real space resolution of 2.1 Å [8]. The high-resolution porous network distinguished by two Zn triplets with spatial resolution 3.3 Å represented by {431} Bragg plane can be resolved up to cumulative dose of 11 $e^{-}Å^{-2}$. The {211} Bragg plane with a spatial resolution of 6.5 Å could be resolved up to cumulative dose of 24 $e^{-}Å^{-2}$. The HRTEM image shown in the left inset in fig. 1(a) shows {211} Bragg spot with a spatial resolution of 6.5 Å with cumulative dose around 19 $eÅ^{-2}$, which is much below the critical dose of the {211} Bragg plane. Hence, the critical dose estimated from the fading of relative intensity of Bragg planes such as {110} and {211} from our diffraction studies matches well with the Bragg planes resolved in experimental HRTEM imaging. The SNR ratio of the HRTEM image of ZIF-8 is relatively poor due to the limitation of the sensitivity of the camera. The use of DDEC camera with high sensitivity and low SNR has shown improved HRTEM image resolution when imaging ZIF-8 [8].

Lowering the dose-rate during the HRTEM imaging process is one of the best practices to protect the sample from electron beam damage. Different materials respond differently with varying dose rates. In dose-rate dependent materials, the electron-beam-induced damage increases with increasing dose rate. Radiolysis, heating, and charging are common damage mechanisms in case of MOFs, zeolites, and organic compounds[45]. In ZIF-8 we didn't find a dose-rate dependency of the critical dose, at least in the range of dose rates from 0.33 to 2 $e^{-}Å^{-2}s^{-1}$ studied here, as shown in our results in fig. 3(b). The number of electrons interacting with the sample in unit time seems not to affect the damage mechanism in ZIF-8. The cumulative dose on the material is more significant. Once the cumulative dose exceeds a threshold value, the ZIF-8 loses its crystallinity[28]. The smaller current density over a long exposure will have the same effect as high current density over a short exposure. Hence, the dose rate around 0.1 $e^{-}Å^{-2}s^{-1}$ can be used during any pre-imaging process in the HRTEM experiment to keep the cumulative dose low. The pre-imaging process consists of three stages; 1. Initial TEM sample screening in low magnification to find the right particle, 2. Zone axis alignment in diffraction space and 3. Focusing for taking the HRTEM image. The high dose over short exposure time should be used during image acquisition with a dose rate of around 1-5 $e^{-}Å^{-2}s^{-1}$.

Our study shows that higher accelerating voltage is more suitable in mitigating beam induced damage. The critical dose of {431} and {110} Bragg planes improves by a factor of 1.29 and 2.79 by increasing the accelerating voltage from 200 to 300 keV. The interaction cross-section is smaller at higher accelerating voltage, which helps in reducing the radiolysis damage[45][46].

ZIF-8 is non-conducting in nature which could lead to sample charging and heating in a TEM experiment. To reduce the effect of charging, conducting substrates such as single layer graphene can be used. A graphene substrate or a graphene encapsulation can lower the electronic excitation generated by the interaction of the incident electrons with the materials, which leads to reduction in electron beam damage [27][47]. We also used holey carbon [48] and single layer graphene substrate to investigate the effect of the substrate material on the loss in crystallinity of ZIF-8. In our experiments, no significant effect of using graphene substrate has been observed. The probable reason could be a minimal adhesion between the ZIF-8 and the graphene substrate [49].

Cooling at cryogenic temperature improves the critical dose of {431} and {110} Bragg plane by a factor of 1.5 and 1.6 as compared to room temperature measurement at 300 keV. Whereas the improvement at 200 keV is 1.1 and 1.4 times for {431} and {110} Bragg planes. Lowering the temperature is effective in

enhancing dose tolerance as it mitigates the impact of sample heating. By reducing the diffusion of secondary radicals generated during electron beam interaction, cooling helps minimize the underlying damage mechanism[50][45]. The formation of thick ice crystals can induce sample drift and also reduce signal-to-noise during imaging[23]. On the other hand, increasing the temperature to 125°C decreased the critical dose of {431} and {110} Bragg plane by a factor of 0.64 and 0.73, respectively, as compared to RT measurement at 300 keV. The contribution from the higher lattice vibration at elevated temperatures promotes bond breaking and leads to a reduction in the critical dose [46]. No significant effect of sample drying in vacuum was observed.

Conclusion:

In this study, we quantitatively investigated the critical dose tolerance of ZIF-8 using fading intensity of Bragg spots in diffraction space and verified with displacement of Bragg planes method. Measurement of the critical dose of {110} Bragg plane from both methods provides relatively close values. The measurement of the critical doses and relative displacement of different planes measurement provides further information about the mechanism of loss of ZIF-8's crystallinity as a function of critical cumulated electron dose. The high index planes, such as {431} with a lower number of ZnN_4 tetrahedra per unit cell, collapse twice as fast compared to {110} planes. The critical dose to break Zn-N bonds in one ZnN_4 tetrahedra is consistent across Bragg planes at about 2.96 ± 0.85 $e^{-}Å^{-2}$, indicating simultaneous bond rupture throughout the crystal, confirming that the radiolysis damage mechanism will be dominate in TEM imaging experiments as well as in other electron-beam processes such as EBL. The critical dose limit to resolve 6MR gate or aperture during HRTEM imaging without introducing any lattice displacement is around 9 $e^{-}Å^{-2}$. ZIF-8 seems to be a dose-rate independent material. Once the cumulative dose exceeds a threshold value, ZIF-8 loses its crystallinity.

Hence, for HRTEM image acquisition an electron dose rate of about 1-5 $e^{-}Å^{-2}s^{-1}$ over short exposure time of few seconds should be used. A higher accelerating voltage, preferably 300 keV is more suitable for reducing beam-induced damage. No significant effect of using graphene as a conducting substrate was observed at any accelerating voltage. Using cryo temperatures seems to mitigate the electron beam induced damage and improves the critical dose considerably, as compared to room temperature measurement at 300 keV. No significant effect of sample drying in vacuum has been observed.

Acknowledgement:

J.R.J acknowledges funding from the Novo Nordisk Foundation (Project "Electron Microscopy of Dynamical Processes", NNF21OC0072844) and P.B. acknowledge support by VILLUM FONDEN (Project "Stabilization of few-atom metal catalysts in 3D nano-cage architecture for conversion of CO_2 into high-value hydrocarbon", grant number 58844). P.B. wishes to thank Prof. Thomas Willum Hansen and Associate Prof. Paul Kempen from DTU Nanolab for their invaluable assistance in conducting the heating and cryo TEM experiments, as well as Prof. Stig Helveg from DTU Physics / VISION Center for invaluable discussions during data analysis.

References

[1] A. Elaouni, M. El Ouardi, M. Zbair, A. BaQais, M. Saadi, and H. Ait Ahsaine, "ZIF-8 metal organic framework materials as a superb platform for the removal and photocatalytic degradation of organic pollutants: a review," *RSC Adv.*, vol. 12, no. 49, pp. 31801–31817, 2022, doi: 10.1039/D2RA05717D.

[2] C. Zhang, R. P. Lively, K. Zhang, J. R. Johnson, O. Karvan, and W. J. Koros, "Unexpected Molecular Sieving Properties of Zeolitic Imidazolate Framework-8," *J. Phys. Chem. Lett.*, vol. 3, no. 16, pp. 2130–2134, Aug. 2012, doi: 10.1021/jz300855a.

[3] M. Bergaoui, M. Khalfaoui, A. Awadallah-F, and S. Al-Muhtaseb, "A review of the features and applications of ZIF-8 and its derivatives for separating CO2 and isomers of C3- and C4-hydrocarbons," *J. Nat. Gas Sci. Eng.*, vol. 96, p. 104289, Dec. 2021, doi: 10.1016/j.jngse.2021.104289.

[4] K. S. Park *et al.*, "Exceptional chemical and thermal stability of zeolitic imidazolate frameworks," *Proc. Natl. Acad. Sci.*, vol. 103, no. 27, pp. 10186–10191, Jul. 2006, doi: 10.1073/pnas.0602439103.

[5] Q. Song *et al.*, "Zeolitic imidazolate framework (ZIF-8) based polymer nanocomposite membranes for gas separation," *Energy Environ. Sci.*, vol. 5, no. 8, p. 8359, 2012, doi: 10.1039/c2ee21996d.

[6] R. Makiura, S. Motoyama, Y. Umemura, H. Yamanaka, O. Sakata, and H. Kitagawa, "Surface nano-architecture of a metal–organic framework," *Nat. Mater.*, vol. 9, no. 7, pp. 565–571, Jul. 2010, doi: 10.1038/nmat2769.

[7] Z. Fang, B. Bueken, D. E. De Vos, and R. A. Fischer, "Defect-Engineered Metal–Organic Frameworks," *Angew. Chemie Int. Ed.*, vol. 54, no. 25, pp. 7234–7254, Jun. 2015, doi: 10.1002/anie.201411540.

[8] Y. Zhu *et al.*, "Unravelling surface and interfacial structures of a metal–organic framework by transmission electron microscopy," *Nat. Mater.*, vol. 16, no. 5, pp. 532–536, May 2017, doi: 10.1038/nmat4852.

[9] M. Zahmakiran, "Iridium nanoparticles stabilized by metal organic frameworks (IrNPs@ZIF-8): Synthesis, structural properties and catalytic performance," *Dalt. Trans.*, 2012, doi: 10.1039/c2dt31779f.

[10] D. Esken, S. Turner, O. I. Lebedev, G. Van Tendeloo, and R. A. Fischer, "Au@ZIFs: Stabilization and Encapsulation of Cavity-Size Matching Gold Clusters inside Functionalized Zeolite Imidazolate Frameworks, ZIFs," *Chem. Mater.*, vol. 22, no. 23, pp. 6393–6401, Dec. 2010, doi: 10.1021/cm102529c.

[11] K. L. Kollmannsberger, L. Kronthaler, J. R. Jinschek, and R. A. Fischer, "Defined metal atom aggregates precisely incorporated into metal–organic frameworks," *Chem. Soc. Rev.*, vol. 51, no. 24, pp. 9933–9959, 2022, doi: 10.1039/D1CS00992C.

[12] K. Kratzl *et al.*, "Generation and Stabilization of Small Platinum Clusters Pt 12± x Inside a Metal–Organic Framework," *J. Am. Chem. Soc.*, vol. 141, no. 35, pp. 13962–13969, Sep. 2019, doi: 10.1021/jacs.9b07083.

[13] K. L. Kollmannsberger *et al.*, "Mechanistic Insights into ZIF-8 Encapsulation of Atom-Precise Pt(M) Carbonyl Clusters," *Chem. Mater.*, vol. 35, no. 14, pp. 5475–5486, Jul. 2023, doi:

10.1021/acs.chemmater.3c00807.

[14] M. Tu *et al.*, "Direct X-ray and electron-beam lithography of halogenated zeolitic imidazolate frameworks," *Nat. Mater.*, vol. 20, no. 1, pp. 93–99, Jan. 2021, doi: 10.1038/s41563-020-00827-x.

[15] Y. Miao and M. Tsapatsis, "Electron Beam Patterning of Metal–Organic Frameworks," *Chem. Mater.*, vol. 33, no. 2, pp. 754–760, Jan. 2021, doi: 10.1021/acs.chemmater.0c04204.

[16] S. Conrad *et al.*, "Controlling Dissolution and Transformation of Zeolitic Imidazolate Frameworks by using Electron-Beam-Induced Amorphization," *Angew. Chemie Int. Ed.*, vol. 57, no. 41, pp. 13592–13597, Oct. 2018, doi: 10.1002/anie.201809921.

[17] Y. Zhu, Q. Wang, L. Zhao, B. Teng, W. Lu, and Y. Han, "Atomic resolution imaging of nanoscale structural ordering in a complex metal oxide catalyst," *Chem. Mater.*, 2012, doi: 10.1021/cm301828n.

[18] A. Zheng, K. Yin, R. Pan, M. Zhu, Y. Xiong, and L. Sun, "Research Progress on Metal–Organic Frameworks by Advanced Transmission Electron Microscopy," *Nanomaterials*, vol. 13, no. 11, p. 1742, May 2023, doi: 10.3390/nano13111742.

[19] J. Zhang, N. Cheng, and B. Ge, "Characterization of metal-organic frameworks by transmission electron microscopy," *Adv. Phys. X*, vol. 7, no. 1, Dec. 2022, doi: 10.1080/23746149.2022.2046157.

[20] S. Turner, O. I. Lebedev, F. Schröder, D. Esken, R. A. Fischer, and G. Van Tendeloo, "Direct Imaging of Loaded Metal−Organic Framework Materials (Metal@MOF-5)," *Chem. Mater.*, vol. 20, no. 17, pp. 5622–5627, Sep. 2008, doi: 10.1021/cm801165s.

[21] C. Wiktor, S. Turner, D. Zacher, R. A. Fischer, and G. Van Tendeloo, "Imaging of intact MOF-5 nanocrystals by advanced TEM at liquid nitrogen temperature," *Microporous Mesoporous Mater.*, vol. 162, pp. 131–135, Nov. 2012, doi: 10.1016/j.micromeso.2012.06.014.

[22] Z. Huang, T. Willhammar, and X. Zou, "Three-dimensional electron diffraction for porous crystalline materials: structural determination and beyond," *Chem. Sci.*, vol. 12, no. 4, pp. 1206–1219, 2021, doi: 10.1039/D0SC05731B.

[23] X. Li *et al.*, "Electron counting and beam-induced motion correction enable near-atomic-resolution single-particle cryo-EM," *Nat. Methods*, vol. 10, no. 6, pp. 584–590, Jun. 2013, doi: 10.1038/nmeth.2472.

[24] I. Lazić, E. G. T. Bosch, and S. Lazar, "Phase contrast STEM for thin samples: Integrated differential phase contrast," *Ultramicroscopy*, vol. 160, pp. 265–280, Jan. 2016, doi: 10.1016/j.ultramic.2015.10.011.

[25] Y. Li *et al.*, "Cryo-EM Structures of Atomic Surfaces and Host-Guest Chemistry in Metal-Organic Frameworks," *Matter*, vol. 1, no. 2, pp. 428–438, Aug. 2019, doi: 10.1016/j.matt.2019.06.001.

[26] J. P. Patterson *et al.*, "Observing the Growth of Metal–Organic Frameworks by in Situ Liquid Cell Transmission Electron Microscopy," *J. Am. Chem. Soc.*, vol. 137, no. 23, pp. 7322–7328, Jun. 2015, doi: 10.1021/jacs.5b00817.

[27] N. Jain *et al.*, "Exploring the effects of graphene and temperature in reducing electron beam damage: A TEM and electron diffraction-based quantitative study on Lead Phthalocyanine (PbPc) crystals," *Micron*, vol. 169, no. January, p. 103444, Jun. 2023, doi: 10.1016/j.micron.2023.103444.

[28] S. Ghosh, H. Yun, P. Kumar, S. Conrad, M. Tsapatsis, and K. A. Mkhoyan, "Two Distinct Stages of Structural Modification of ZIF-L MOF under Electron-Beam Irradiation," *Chem. Mater.*, vol. 33, no. 14, pp. 5681–5689, 2021, doi: 10.1021/acs.chemmater.1c01332.

[29] Z. J. W. A. Leijten, A. D. A. Keizer, G. de With, and H. Friedrich, "Quantitative Analysis of Electron Beam Damage in Organic Thin Films," *J. Phys. Chem. C*, vol. 121, no. 19, pp. 10552–10561, May 2017, doi: 10.1021/acs.jpcc.7b01749.

[30] M. Ilett *et al.*, "Analysis of complex, beam-sensitive materials by transmission electron microscopy and associated techniques," *Philos. Trans. R. Soc. A Math. Phys. Eng. Sci.*, vol. 378, no. 2186, p. 20190601, Dec. 2020, doi: 10.1098/rsta.2019.0601.

[31] T. Ueda, T. Yamatani, and M. Okumura, "Dynamic Gate Opening of ZIF-8 for Bulky Molecule Adsorption as Studied by Vapor Adsorption Measurements and Computational Approach," *J. Phys. Chem. C*, vol. 123, no. 45, pp. 27542–27553, Nov. 2019, doi: 10.1021/acs.jpcc.9b07239.

[32] Q. Hou, Y. Wu, S. Zhou, Y. Wei, J. Caro, and H. Wang, "Ultra-Tuning of the Aperture Size in Stiffened ZIF-8_Cm Frameworks with Mixed-Linker Strategy for Enhanced CO 2 /CH 4 Separation," *Angew. Chemie Int. Ed.*, vol. 58, no. 1, pp. 327–331, Jan. 2019, doi: 10.1002/anie.201811638.

[33] K. Momma and F. Izumi, "VESTA 3 for three-dimensional visualization of crystal, volumetric and morphology data," *J. Appl. Crystallogr.*, vol. 44, no. 6, pp. 1272–1276, 2011, doi: 10.1107/S0021889811038970.

[34] W. R. K. Clark, J. N. Chapman, A. M. MacLeod, and R. P. Ferrier, "Radiation damage mechanisms in copper phthalocyanine and its chlorinated derivatives," *Ultramicroscopy*, vol. 5, no. 1–3, pp. 195–208, Jan. 1980, doi: 10.1016/0304-3991(80)90024-8.

[35] D. T. Grubb, "Radiation damage and electron microscopy of organic polymers," *J. Mater. Sci.*, vol. 9, no. 10, pp. 1715–1736, Oct. 1974, doi: 10.1007/BF00540772.

[36] S. H. w. Scheres, "Beam-induced motion correction for sub-megadalton cryo-EM particles," *Elife*, vol. 3, Aug. 2014, doi: 10.7554/eLife.03665.

[37] A. F. Brilot *et al.*, "Beam-induced motion of vitrified specimen on holey carbon film," *J. Struct. Biol.*, 2012, doi: 10.1016/j.jsb.2012.02.003.

[38] W.-H. Lai, G.-L. Zhuang, H.-H. Tseng, and M.-Y. Wey, "Creation of tiny defects in ZIF-8 by thermal annealing to improve the CO2/N2 separation of mixed matrix membranes," *J. Memb. Sci.*, vol. 572, pp. 410–418, Feb. 2019, doi: 10.1016/j.memsci.2018.11.010.

[39] J. B. James and Y. S. Lin, "Kinetics of ZIF-8 Thermal Decomposition in Inert, Oxidizing, and Reducing Environments," *J. Phys. Chem. C*, 2016, doi: 10.1021/acs.jpcc.6b01208.

[40] S. Gadipelli, W. Travis, W. Zhou, and Z. Guo, "A thermally derived and optimized structure from ZIF-8 with giant enhancement in CO 2 uptake," *Energy Environ. Sci.*, vol. 7, no. 7, pp. 2232–2238, 2014, doi: 10.1039/C4EE01009D.

[41] B. Zheng, L. L. Wang, J. C. Hui, L. Du, H. Du, and M. Zhu, "Impact of mechanical deformation on guest diffusion in zeolitic imidazolate frameworks," *Dalt. Trans.*, vol. 45, no. 10, pp. 4346–4351, 2016, doi: 10.1039/C5DT03861H.

[42] C. Han, C. Zhang, N. Tymińska, J. R. Schmidt, and D. S. Sholl, "Insights into the Stability of Zeolitic Imidazolate Frameworks in Humid Acidic Environments from First-Principles Calculations," *J. Phys. Chem. C*, vol. 122, no. 8, pp. 4339–4348, Mar. 2018, doi:

10.1021/acs.jpcc.7b12058.

[43] S. Bhattacharyya *et al.*, "Acid Gas Stability of Zeolitic Imidazolate Frameworks: Generalized Kinetic and Thermodynamic Characteristics," *Chem. Mater.*, vol. 30, no. 12, pp. 4089–4101, Jun. 2018, doi: 10.1021/acs.chemmater.8b01394.

[44] R. Han, N. Tymińska, J. R. Schmidt, and D. S. Sholl, "Propagation of Degradation-Induced Defects in Zeolitic Imidazolate Frameworks," *J. Phys. Chem. C*, 2019, doi: 10.1021/acs.jpcc.9b00304.

[45] R. F. Egerton, "Radiation damage to organic and inorganic specimens in the TEM," *Micron*, vol. 119, no. November 2018, pp. 72–87, Apr. 2019, doi: 10.1016/j.micron.2019.01.005.

[46] J. Cattle, M. S'ari, N. Hondow, P. Abellán, A. P. Brown, and R. M. D. Brydson, "Transmission electron microscopy of a model crystalline organic, theophylline," *J. Phys. Conf. Ser.*, vol. 644, p. 012030, Oct. 2015, doi: 10.1088/1742-6596/644/1/012030.

[47] N. Mohanty, M. Fahrenholtz, A. Nagaraja, D. Boyle, and V. Berry, "Impermeable Graphenic Encasement of Bacteria," *Nano Lett.*, vol. 11, no. 3, pp. 1270–1275, Mar. 2011, doi: 10.1021/nl104292k.

[48] J. Brink, M. B. Sherman, J. Berriman, and W. Chiu, "Evaluation of charging on macromolecules in electron cryomicroscopy," *Ultramicroscopy*, vol. 72, no. 1–2, pp. 41–52, Apr. 1998, doi: 10.1016/S0304-3991(97)00126-5.

[49] S. Sinha and J. H. Warner, "Recent Progress in Using Graphene as an Ultrathin Transparent Support for Transmission Electron Microscopy," *Small Structures*. 2021. doi: 10.1002/sstr.202000049.

[50] J. R. Fryer, C. H. McConnell, F. Zemlin, and D. L. Dorset, "Effect of temperature on radiation damage to aromatic organic molecules," *Ultramicroscopy*, 1992, doi: 10.1016/0304-3991(92)90057-Q.

Supplementary Information:

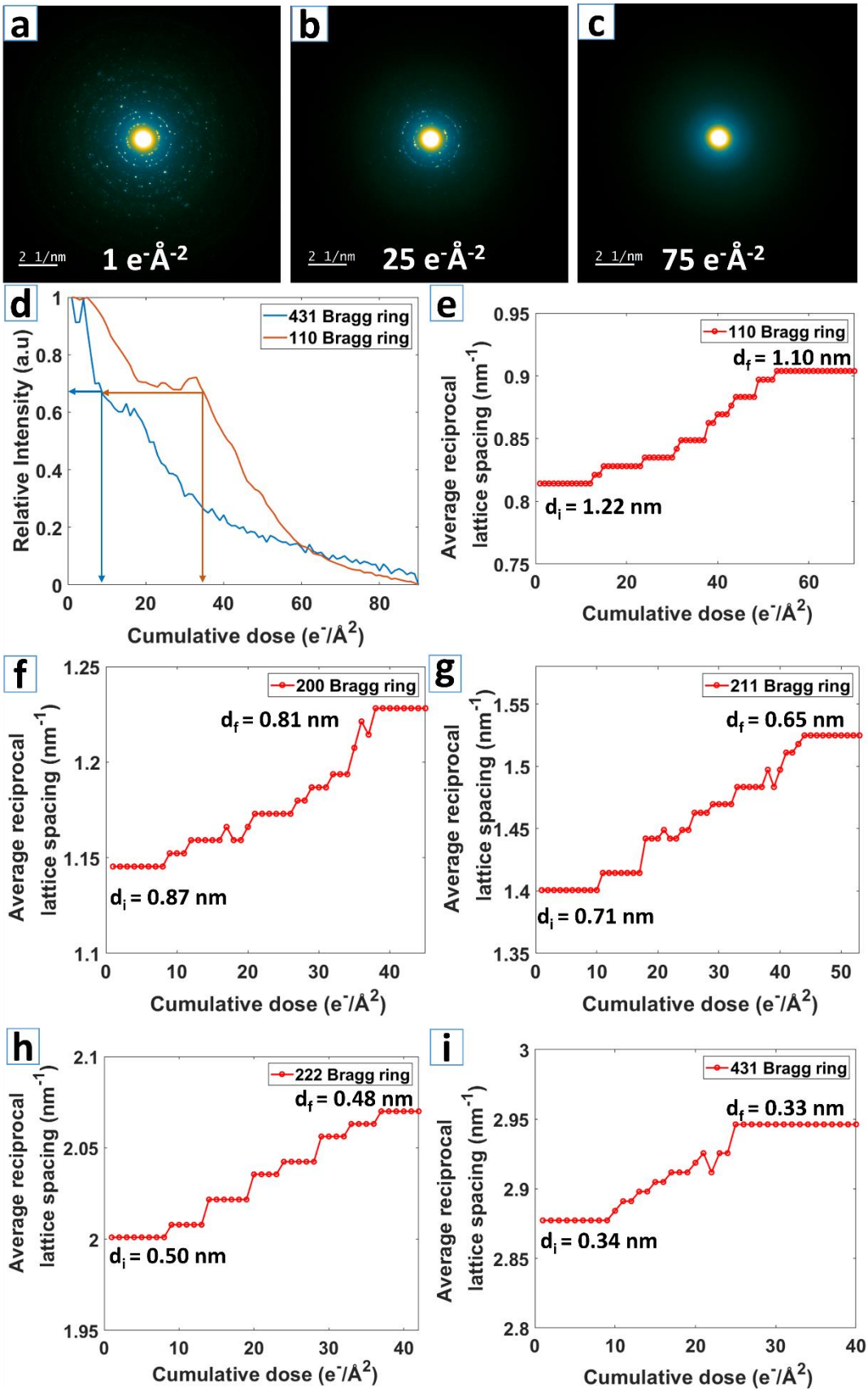

Fig. S1 (a-c) Diffraction patterns of ZIF-8 acquired at a dose rate of 1 $e^{-}Å^{-2}s^{-1}$ with cumulative dose of 1, 25 and 75 $e^{-}Å^{-2}$, respectively. (d) Plot showing the fading of relative intensity of 431 and 110 Bragg ring as a function of cumulative dose at 300 keV at dose rate of 1 $e^{-}Å^{-2}s^{-1}$. (e-i) Average reciprocal lattice spacing of 110, 200, 211, 222 and 431 Bragg plane as a function of cumulative dose.

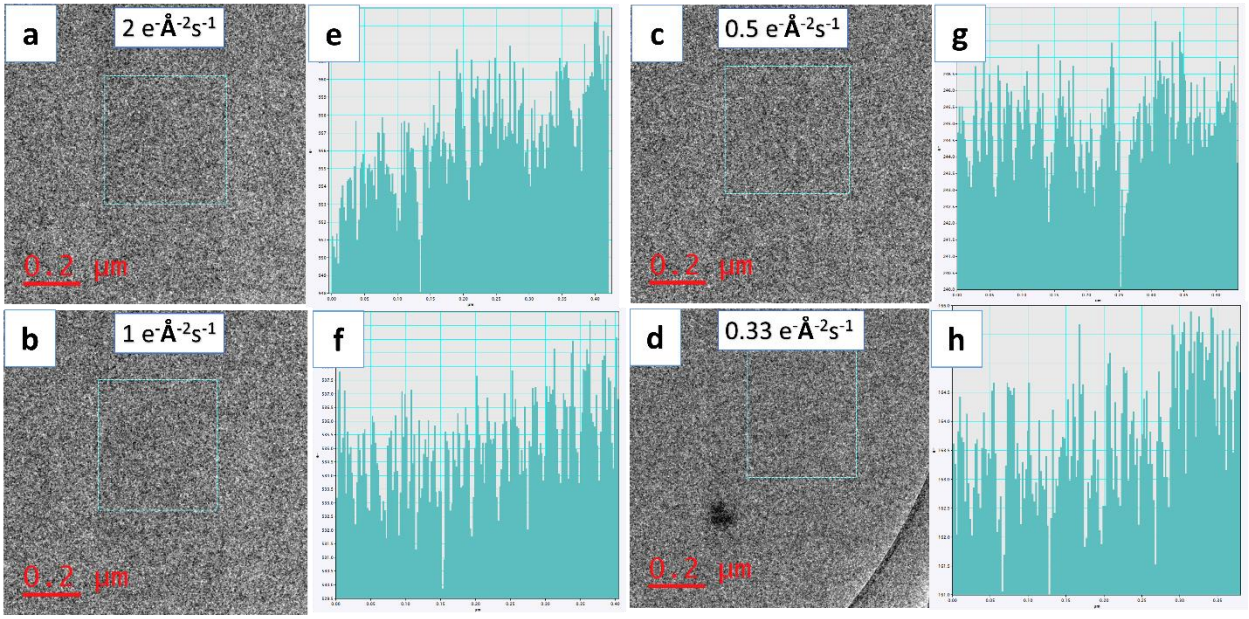

Fig. S2(a-d) Phase contrast images of the electron beam in the vacuum region with varying beam current and corresponding dose rates of 2, 1, 0.5, 0.33 $e^{-}Å^{-2}s^{-1}$, respectively. (e-h) The corresponding line profiles of electron counts per sec or beam currents.

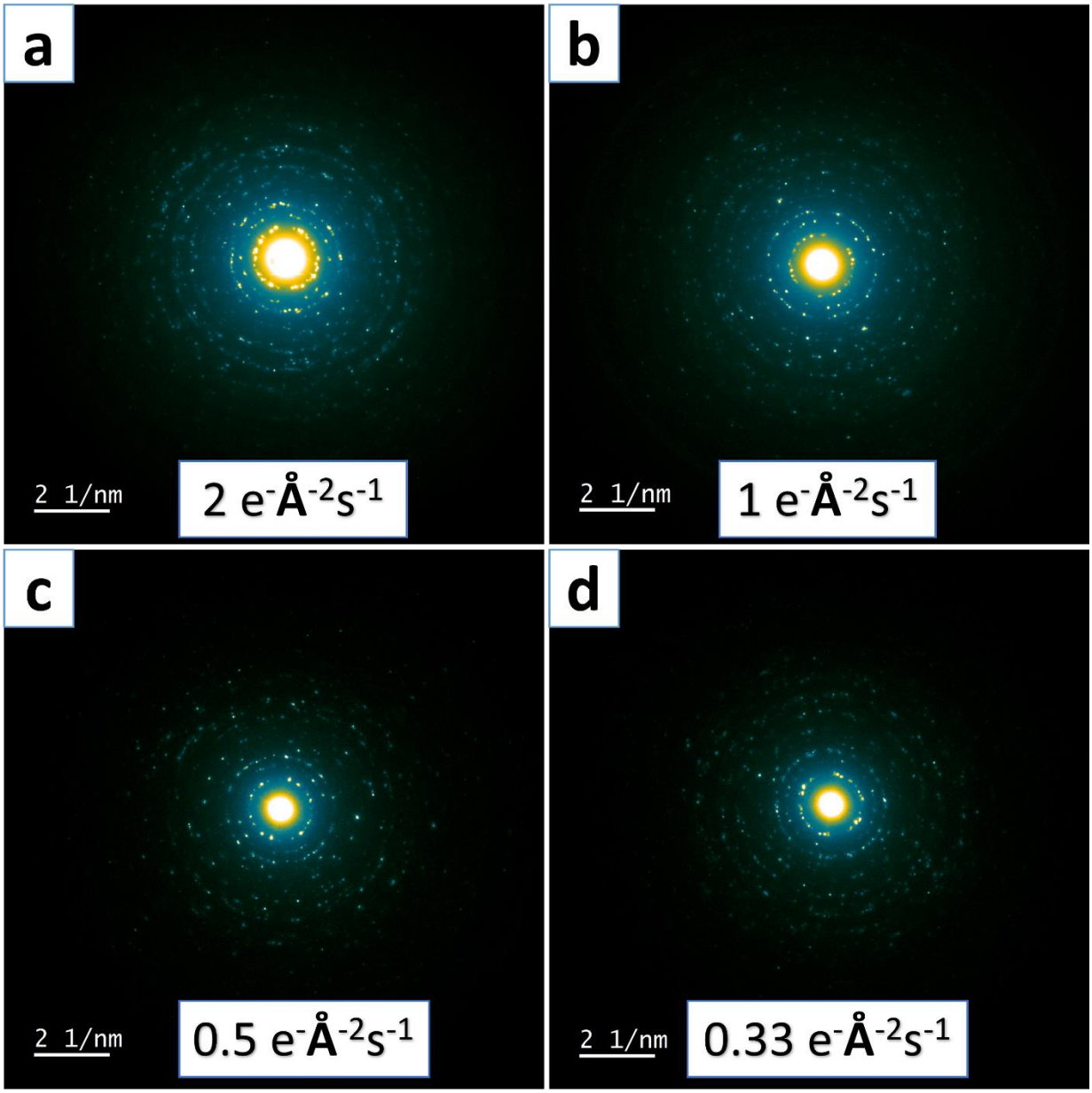

Fig. S3(a-d) Electron diffraction patterns of ZIF-8 acquired at different electron dose rates of 2, 1, 0.5 and 0.3 $e^{-}Å^{-2}s^{-1}$ respectively at 300 keV.

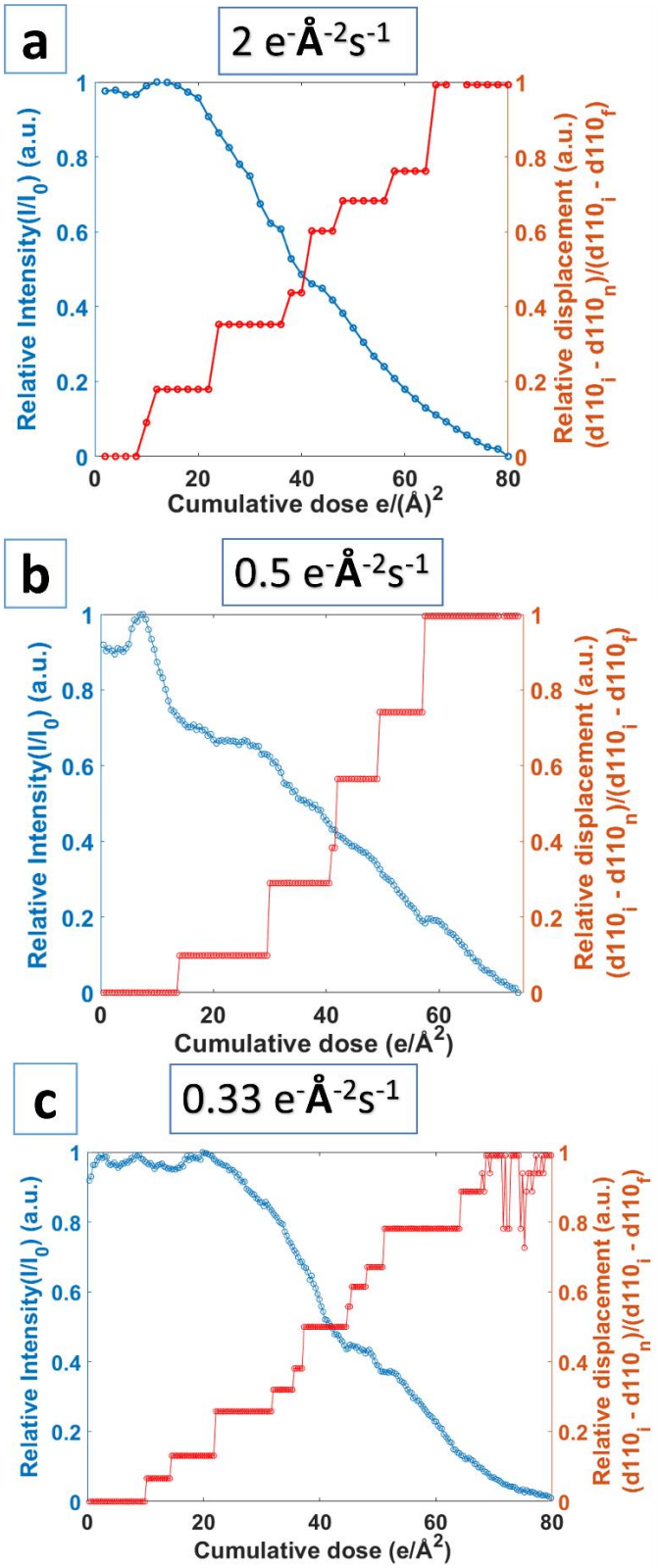

Fig. S4 (a-c) *Fading of relative intensity and relative displacement of 110 Bragg plane with cumulative dose with varying dose rates of 2, 0.5 and 0.33 $e^{-}Å^{-2}s^{-1}$ respectively at 300 keV.*

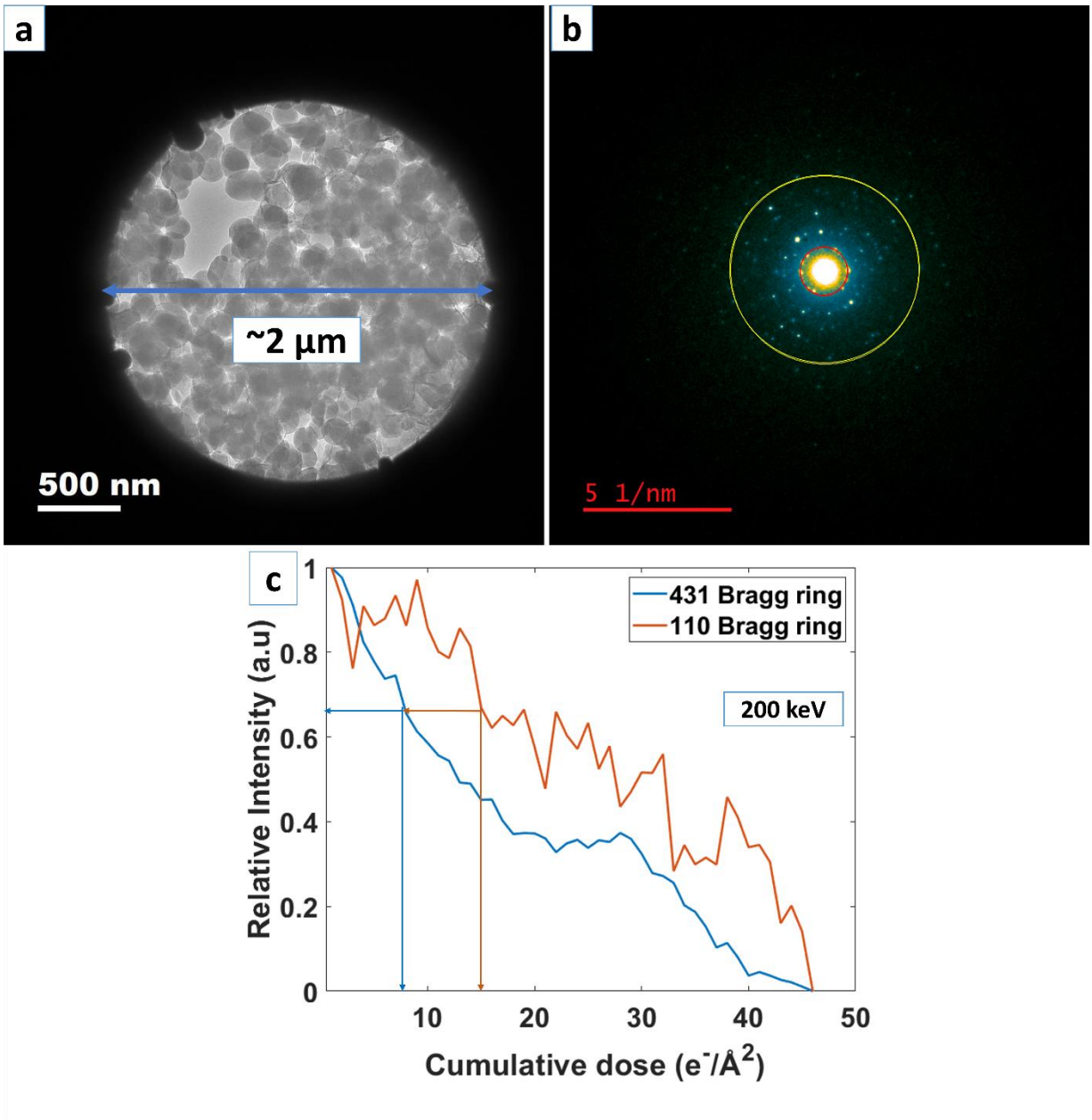

Fig. S5(a) Low magnification phase contrast TEM image of the ZIF-8 particles with a beam diameter of 2 µm and beam current of 0.050 nA at accelerating voltage of 200 keV. (b) Electron diffraction pattern of ZIF-8 supported on holey carbon (c,d) Comparison of fading of relative intensity of 431 and 110 Bragg rings at 200 keV. Critical doses of 431 and 110 planes are represented by the blue and the orange arrow respectively.

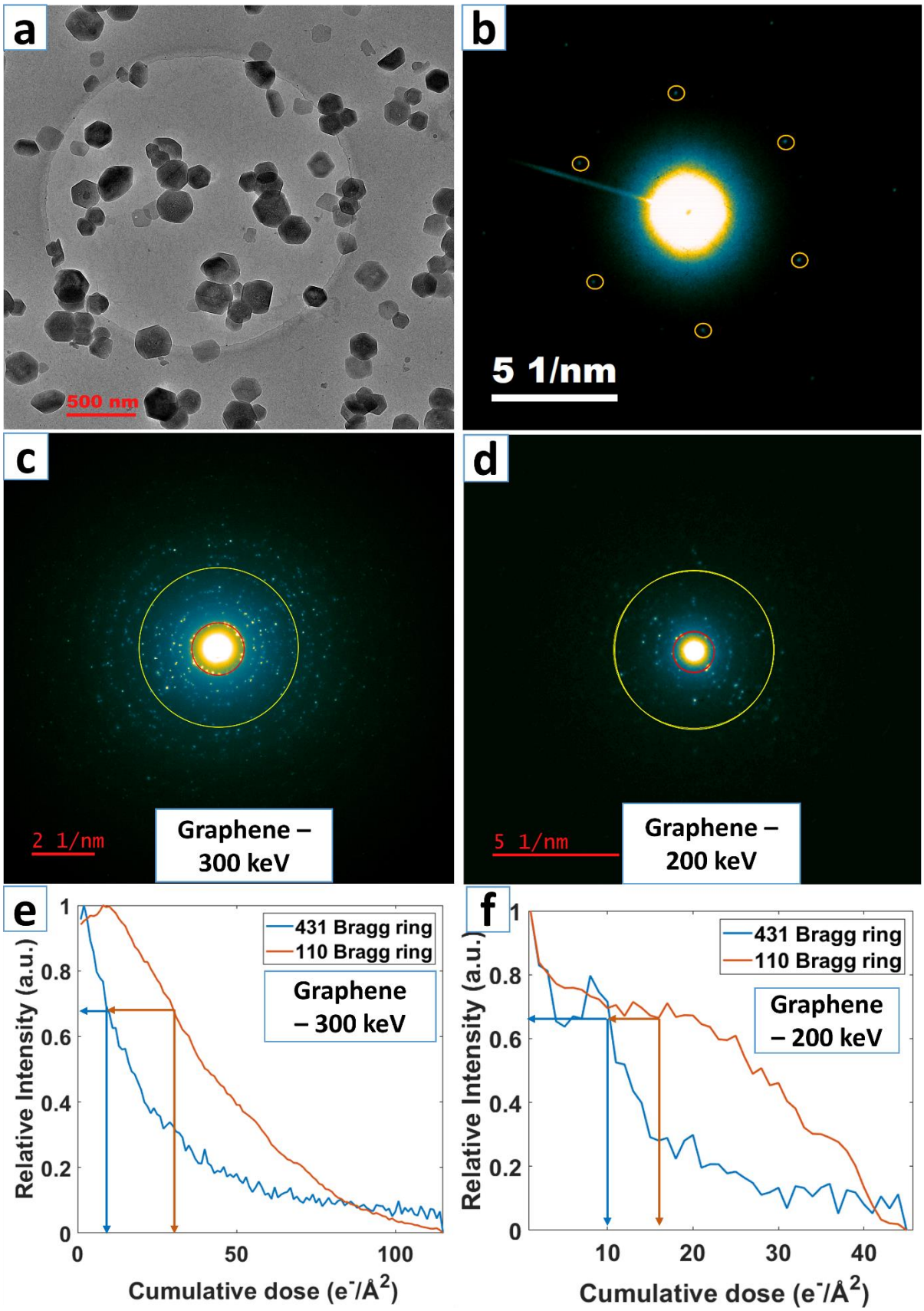

Fig. S6(a) Low magnification phase contrast TEM image of the ZIF-8 particles on graphene substrate. (b) Electron diffraction pattern showing Bragg spots of graphene film with hexagonal symmetry. (c, d) Diffraction pattern of ZIF-8 supported on graphene substrate at 300 and 200 keV respectively. (e, f) Fading of relative intensity of 431 and 110 Bragg ring at 300 and 200 keV, respectively. Critical doses of 431 and 110 planes are represented by the blue and the orange arrow respectively.

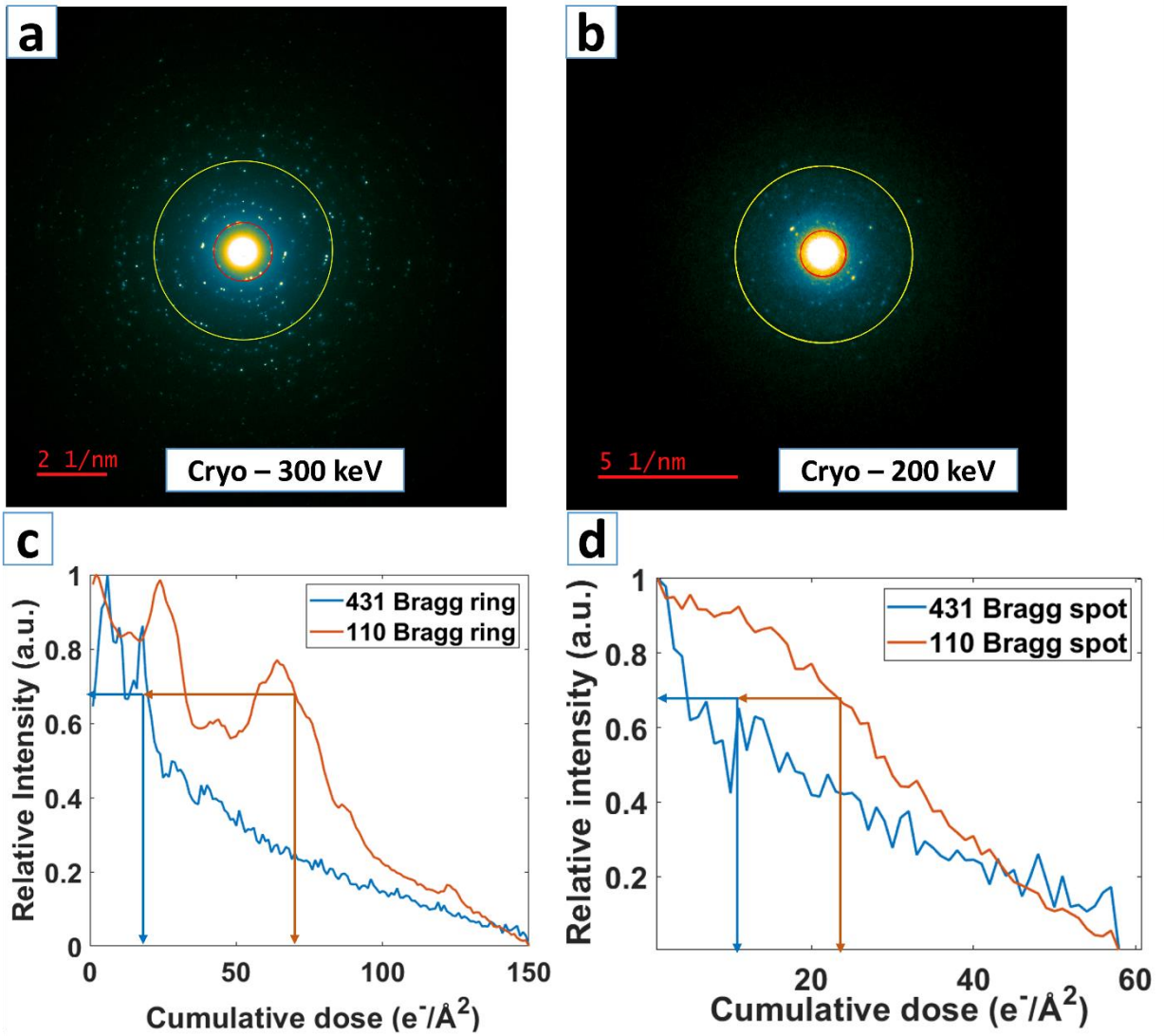

Fig. S7 (a, b) Electron diffraction patterns of ZIF-8 under cryo temperature at 300 and 200 keV respectively. (c, d) Fading of relative intensity of 431 and 110 Bragg ring at 300 and 200 keV respectively under cryo temperature. Critical doses of 431 and 110 planes are represented by the blue and the orange arrow respectively.

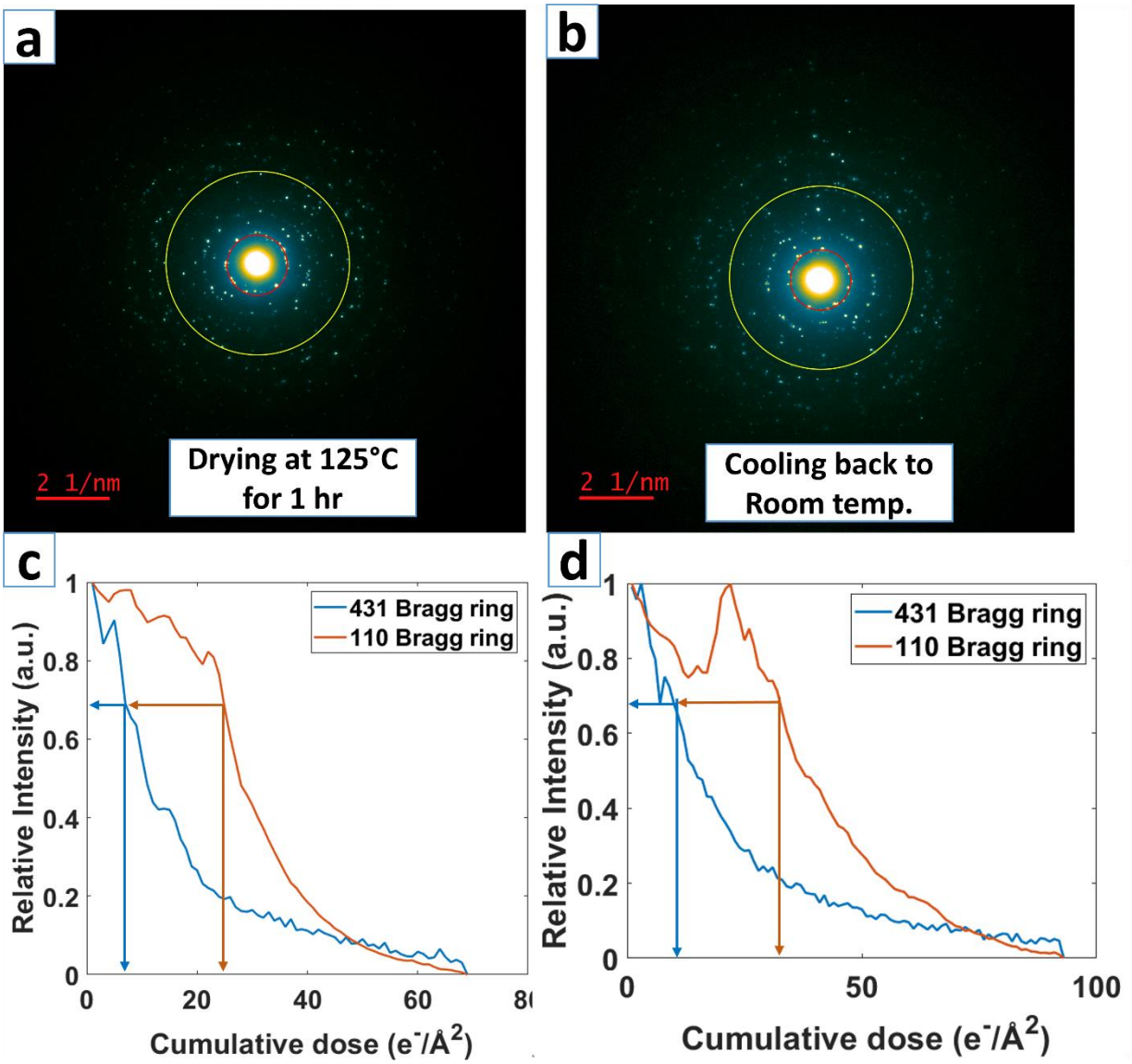

Fig. S8 (a, b) Electron diffraction patterns of ZIF-8 at 125°C and cooled down to RT at 300 keV, respectively. (c, d) Fading of relative intensity of 431 and 110 Bragg ring at 125°C and cooled back down to RT. Critical doses of 431 and 110 planes are represented by the blue and the orange arrow respectively.

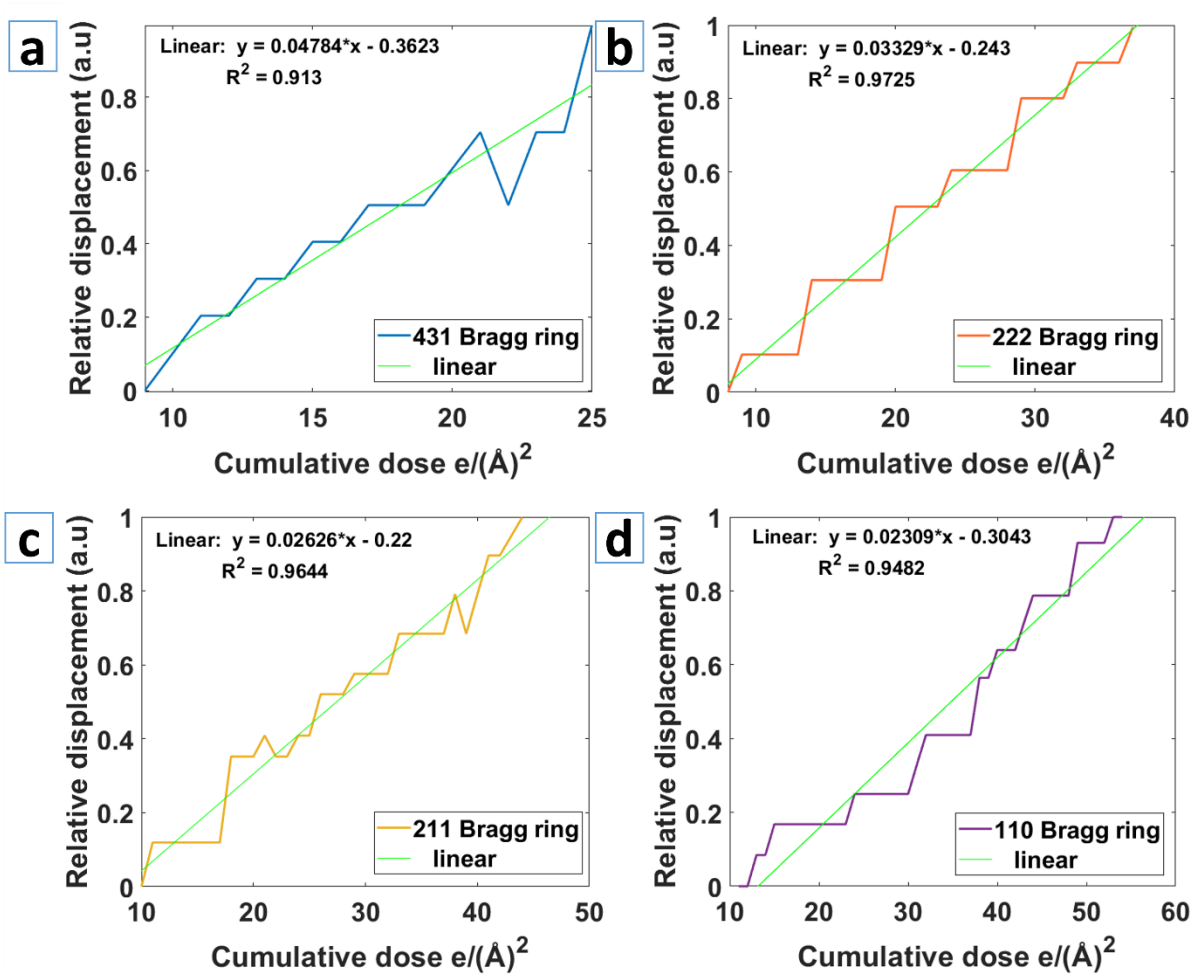

Fig. S9(a-d) Plot of relative displacement of 431, 222, 211 and 110 Bragg plane respectively with linear fitting. The slope determines the rate of change of relative displacement of Bragg planes per unit dose.